

9-3-2010

# 2-D Modeling of Electromagnetic Waves with Vibrating Conducting and Dielectric Objects

Monica Jaramillo-Madrid

Follow this and additional works at: [https://digitalrepository.unm.edu/ece\\_etds](https://digitalrepository.unm.edu/ece_etds)

---

## Recommended Citation

Jaramillo-Madrid, Monica. "2-D Modeling of Electromagnetic Waves with Vibrating Conducting and Dielectric Objects." (2010).  
[https://digitalrepository.unm.edu/ece\\_etds/125](https://digitalrepository.unm.edu/ece_etds/125)

This Thesis is brought to you for free and open access by the Engineering ETDs at UNM Digital Repository. It has been accepted for inclusion in Electrical and Computer Engineering ETDs by an authorized administrator of UNM Digital Repository. For more information, please contact [disc@unm.edu](mailto:disc@unm.edu).

Monica Jaramillo-Madrid

*Chair*

Electrical and Computer Engineering

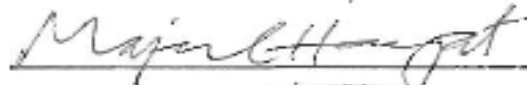
*Department*

This thesis is approved, and it is acceptable in quality  
and form for publication;

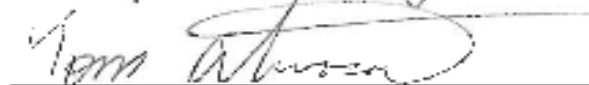
*Approved by the Thesis Committee:*



Jamesina Simpson, Chairperson



Majeed Hayat



Tom Atwood

---

---

---

---

---

---

---

---

**2-D MODELING OF ELECTROMAGNETIC WAVES WITH  
VIBRATING CONDUCTING AND DIELECTRIC OBJECTS**

**BY**

**MONICA JARAMILLO-MADRID**

**BACHELORS  
PSYCHOLOGY/SPANISH, THE UNIVERSITY OF NEW  
MEXICO, 2005**

**THESIS**

Submitted in Partial Fulfillment of the  
Requirements for the Degree of

**Master of Science  
Electrical Engineering**

The University of New Mexico  
Albuquerque, New Mexico

**July 2010**

©2010, Monica Jaramillo-Madrid

## DEDICATION

To my grandparents, Filiberto and Florella Sanchez and Theresa Jaramillo. Thank you for always encouraging and supporting me. It deeply saddens me that none of you will ever get the chance to see me in my profession and what I have accomplished, but I know you are and will always be there in spirit. You will forever be in my heart.

## ACKNOWLEDGMENTS

I am forever indebted to Dr. Jamesina Simpson, my advisor and committee chair, who believed in me and so willingly accepted me as one of her graduate students, even though Electrical Engineering (EE) was not my undergraduate field of study. She has supported me not only in the education of EE but as a female in the field of Engineering. Her patients, intelligence and dedication have inspired me to succeed in my future endeavors in this profession

A special thanks to my committee members, Dr. Majeed Hayat and Dr. Tom Atwood for serving on my M.S. Thesis defense committee. I am truly honored to have the support of two such prestigious professionals.

I extend my deepest gratitude to Deputy Lee Madrid, my husband who has patiently supported me whole-heartedly during this long journey. Thank you so much for the sacrifices you silently endured in order for me to achieve my aspirations. You have been unbelievably amazing to me during this time and words will never explain my appreciation. I am motivated by you to be the best that I can be.

To my parents, Dolores and Roque Jaramillo and my sister, Geneva Jaramillo, thank you for always believing in me and encouraging me the whole way. You guys were persistently there to support me during hard and happy times, reliably turning on the "Angel" light whenever I had a test or a presentation. Your love and guidance has made me the person I am today.

I would like to thank my in-laws for accepting me unconditionally with open-arms and for supporting me in all of my endeavors. All of you were always genuinely concerned and involved with my education and well-being during this time.

Lastly, I would like to acknowledge my four-legged, fur children. All of you always made sure I was walked and well exercised in order to keep me healthy for this long haul. And thank you for the long nights and early mornings of studying and working you all endured with me so loyally, never leaving my side until it was time to go to sleep.

This work was supported by the United States Department of Energy (award no. DE-FG52-08NA28782), the National Science Foundation (award no. IIS-0813747), and Sandia National Laboratories.

Also, a Selected Professions Fellowship from the American Association of University Women was held during 2009-2010.

**2-D MODELING OF ELECTROMAGNETIC WAVES WITH  
VIBRATING CONDUCTING AND DIELECTRIC OBJECTS**

**BY**

**MONICA JARAMILLO-MADRID**

**ABSTRACT OF THESIS**

Submitted in Partial Fulfillment of the  
Requirements for the Degree of

**Master of Science  
Electrical Engineering**

The University of New Mexico  
Albuquerque, New Mexico

**July 2010**

## **2-D MODELING OF ELECTROMAGNETIC WAVES WITH VIBRATING CONDUCTING AND DIELECTRIC OBJECTS**

**Monica Jaramillo-Madrid**

**B.A., Psychology/Spanish, The University of New Mexico, 2005**

**M.S., Electrical Engineering, The University of New Mexico, 2010**

### **ABSTRACT**

This Thesis provides an analysis of the interaction of electromagnetic pulses with vibrating conducting and dielectric objects. Two-dimensional full-vector Maxwell's equations finite-difference time-domain (FDTD) models are employed that include total-field scattered-field incident plane wave source conditions, a frequency domain near-to-far-field transformation, convolutional perfectly matched layer boundary conditions and an advanced surface boundary condition that accommodates the surface perturbations of the vibrating objects. Reflection and diffraction of incident plane waves are calculated for stationary and vibrating objects and the diffraction coefficient for vibrating right-angle corners are obtained. The work of this Thesis may have application to the interaction of radar pulses with buildings having characteristic vibration signatures.



## Table of Contents

List of Figures .....	ix
Chapter 1 Introduction .....	1
1.1 Overview .....	1
1.2 Goals of This Thesis .....	3
Chapter 2 Background.....	5
2.1 Modeling Moving Objects in FDTD Grids .....	5
2.2 Calculation of Diffraction Coefficients.....	6
Chapter 3 FDTD Model Components .....	8
3.1 Introduction of FDTD.....	8
3.2 Introduction of TFSS .....	11
3.3 Introduction of Convolutional Perfectly Matched Layer (CPML) .....	12
3.4 Introduction of the Frequency-Domain Near-to-Far-Field (NTFF) Transformation.....	13
3.5 Modeling Object Vibrations .....	16
3.5.1 Introduction of the Sheet Boundary Condition (SBC).....	16
3.5.2 Formulation .....	16
3.5.3 Validation Study.....	18
3.5.4 Validation Study Results .....	20
3.6 Calculation of the Diffraction Coefficient.....	24
3.6.1 Methodology.....	24
3.6.2 Validation Study.....	25
3.6.3 Validation Study Results .....	28
Chapter 4 Modeling Studies and Results.....	32
4.1 Diffraction Coefficients of Lossless Dielectric Wedges .....	33
4.1.1 Stationary Dielectric Wedges .....	35
4.1.2 Vertically (along the y-axis) Vibrating Dielectric Wedges .....	36
4.1.3 Horizontally (along the x-axis) Vibrating Dielectric Wedges.....	37
4.2 Diffraction Coefficients of Lossy Wedges .....	38
4.2.1 Stationary Lossy Wedges .....	38
4.2.2 Vertically (along the y-axis) Vibrating Lossy Wedges .....	39
4.2.3 Horizontally (along the x-axis) Vibrating Lossy Wedges.....	40
Chapter 5 Conclusion .....	42
Chapter 6 Future Work.....	44
REFERENCES .....	45

## List of Figures

- Figure 1:** TFSF. A sample 2-D FDTD grid illustrating the two regions of modeled fields. Region 2, made up of scattered fields, surrounds region 1, which consists of total-fields. Courtesy of [6]...... 11
- Figure 2:** The PML is on the outer edges of this Figure, and it effectively introduces losses in each of the four directions of the grid. Courtesy of [6]...... 13
- Figure 3:** 2-D  $TM_z$  scattering or radiation geometry utilized to obtain the NTFF in the phasor domain. Courtesy of [6]...... 14
- Figure 4:** A square cylinder with a width and length of  $2.0\lambda$ , a relative permittivity of 2 and an azimuthal angle denoted by  $\phi$  located in the middle of a free space FDTD grid..... 19
- Figure 5:** Results obtained from [1] for the RCS of a square cylinder with a width and length of  $2.0\lambda$ , a relative permittivity of 2, an azimuthal angle denoted by  $\phi$  and at an incident angle of  $0^\circ$ . Courtesy of [4]...... 21
- Figure 6:** Results obtained from the code in this thesis for the RCS of a square cylinder with a width and length of  $2.0\lambda$ , a relative permittivity of 2, an azimuthal angle denoted by  $\phi$  and at an incident angle of  $0^\circ$ . ..... 21
- Figure 7:** RCS of a square cylinder with a width and length of  $2.0\lambda$ , a relative permittivity of 2, an azimuthal angle denoted by  $\phi$  and at an incident angle of  $30^\circ$ . ..... 22
- Figure 8:** RCS of a square cylinder with a width and length of  $2.0\lambda$ , a relative permittivity of 2, an azimuthal angle denoted by  $\phi$  and at an incident angle of  $60^\circ$ . ..... 23
- Figure 9:** RCS of a square cylinder with a width and length of  $2.0\lambda$ , a relative permittivity of 2, an azimuthal angle denoted by  $\phi$  and at an incident angle of  $90^\circ$ . ..... 23
- Figure 10:** Comparison between the SBC vibrating at 7 mm and the brute-force method of physically moving an object 7 mm. .... 24
- Figure 11:** Parameters of the FDTD Grid that computes the Diffraction Coefficient at Point F. .... 26
- Figure 12:** Snapshot at time step 1,000 of an incoming plane wave at  $80^\circ$  propagating towards a square PEC object located at the upper left of the grid. . 28

**Figure 13:** Snapshot at time step 1,300 of the scattering and diffracting of the electric fields once an incoming plane wave at  $80^{\circ}$  interacts with a square PEC object located at the upper left of the grid, and in particular corner A of the PEC object. .... 29

**Figure 14:** Snapshot at time step 1,700 of the scattering and diffracting of the electric fields once an incoming plane wave at  $80^{\circ}$  interacts with a square PEC object located at the upper left of the grid, and in particular corner A of the PEC object. .... 29

**Figure 15:** Snapshot at time step 2,600 of the scattering and diffracting of the electric fields once an incoming plane wave at  $80^{\circ}$  interacts with a square PEC object located at the upper left of the grid, and in particular corner A of the PEC object. .... 30

**Figure 16:** Comparison between the Analytical Solution and the FDTD results for the diffraction coefficient for a PEC object at Point F( $\rho=6.3$ ,  $\phi=262.37^{\circ}$ )..... 31

**Figure 17:** Relative Error between the analytical and FDTD results of the diffraction coefficient..... 31

**Figure 18:** Snapshot at time step 1,000 of an incoming plane wave at  $80^{\circ}$  propagating towards a square dielectric object located at the upper left of the grid..... 33

**Figure 19:** Snapshot at time step 1,300 of the scattering and diffracting of the electric fields once an incoming plane wave at  $80^{\circ}$  interacts with a square dielectric object located at the upper left of the grid, and in particular corner A of the dielectric object..... 34

**Figure 20:** Snapshot at time step 1,700 of the scattering and diffracting of the electric fields once an incoming plane wave at  $80^{\circ}$  interacts with a square dielectric object located at the upper left of the grid, and in particular corner A of the dielectric object..... 34

**Figure 21:** Snapshot at time step 2,600 of the scattering and diffracting of the electric fields once an incoming plane wave at  $80^{\circ}$  interacts with a square dielectric object located at the upper left of the grid, and in particular corner A of the dielectric object..... 35

**Figure 22:** Comparison between the diffraction coefficients for a lossless stationary square dielectric object with a relative permittivity of 2, 5 and 7. .... 36

**Figure 23:** Comparison between the Doppler diffraction coefficients for a lossless square dielectric object vibrating vertically, along the y-axis, with a relative permittivity of 2, 5 and 7. .... 37

**Figure 24:** Comparison between the Doppler diffraction coefficients for a lossless square dielectric object vibrating horizontally, along the x-axis, with a relative permittivity of 2, 5 and 7. .... 38

**Figure 25:** Comparison between the diffraction coefficients for a lossy stationary square dielectric object with a fixed relative permittivity of 7 and a conductivity of 0 and 10. .... 39

**Figure 26:** Comparison between the Doppler diffraction coefficients for a lossy square dielectric object vibrating vertically, along the y-axis, with a fixed relative permittivity of 7 and a conductivity of 0 and 10. .... 40

**Figure 27:** Comparison between the Doppler diffraction coefficients for a lossy square dielectric object vibrating horizontally, along the x-axis, with a fixed relative permittivity of 7 and a conductivity of 0 and 10. .... 41

## Chapter 1

### Introduction

#### 1.1 Overview

Technology for remotely (such as from an airplane) imaging not only spatial information of buildings and structures, but also simultaneously imaging their vibration signatures lends itself to a complex but important research project. Active structures such as buildings containing certain machinery or generators, as well as combustion-based vehicles, and active underground facilities, bear vital characteristic signatures about those activities. As many signatures from structures can be correlated to nuclear proliferation activities, reliably detecting vibration signals could greatly benefit anomaly detection missions at particular sights of interest. Fusing vibration and spatial information will add a new critical dimension to ordinary imagery. If materialized, the vibration information will be placed in a spatial context, adding robustness and accuracy to anomaly detection.

However, fusing spatial and vibration information from different sensors requires co-registration, a challenging task that is often accompanied by inaccuracies that may compromise any nonproliferation missions. *Presently, no single sensing platform exists that allows the simultaneous generation of imagery and a corresponding two-dimensional array of vibration spectrograms.* Synthetic aperture radar (SAR) poses itself as a natural fit to this problem since (1) it has already been proven as a highly effective imaging technology, and (2) it is

inherently capable of sensing Doppler shifts in the electromagnetic (EM) returns from objects, thereby allowing the detection of vibrations.

The work of this Thesis is in support of an overall goal of designing SAR imaging strategies that yield two-dimensional (spatial) maps of vibration frequencies (spectrograms) superimposed on ordinary SAR images. This process involves transmitting a series of probing EM pulses towards vibrating targets and developing post-processing algorithms that will unambiguously estimate the vibrations at each spot on the ground from the radar returns.

Specifically, this Thesis contributes to the overall project by obtaining an improved understanding of the interaction of EM pulses with vibrating targets by utilizing the finite-difference time-domain (FDTD) method [1,2] to model EM wave interactions with vibrating conducting and dielectric objects. Two-dimensional (2-D), Transverse Magnetic ( $TM_z$ ) FDTD models generated from scratch are employed. These models contain: (1) a Total-Field Scattered-Field (TFSF) incident plane wave formulation to simulate the nearly planar pulsed radar signal incident on structures from remote antennas located at any angle; (2) a Convolutional Perfectly Matched Layer (CPML) [3] boundary condition to prevent unwanted reflections from the outer grid boundaries; (3) a frequency-domain Near-to-Far-Field (NTFF) transformation to compute far-field data (as would be recorded by a remote receiving antenna) from the near-field FDTD-calculated electric and magnetic fields; and (4) an advanced surface boundary condition (SBC) that simulates the boundary perturbations of structures [4,5].

## 1.2 Goals of This Thesis

This Thesis focuses on the interaction of EM radar pulses with vibrating square targets having different material properties, as well as with the corners of specific targets. Using the above full-vector Maxwell's equations FDTD models, the incident, reflected and diffracted EM waves are calculated for each target scenario. This includes calculation of the diffraction coefficient for the corners of both stationary and boundary-perturbed objects. Further, a methodology for obtaining the far-field Doppler component radar cross section (RCS) is presented.

The immediate goal for the work of this Thesis is to attain an advanced comprehension of the interaction of EM radar pulses with vibrating targets in order to aid with the development of the SAR imaging strategies discussed in Section 1.1. As part of future work, as discussed in Chapter 6, the 2-D TM FDTD models of this Thesis will be expanded to three-dimensions (3-D) and utilized to replicate a realistic SAR imaging scenario. That is, modeled 3-D targets located on the ground will be excited by incident plane waves as would originate from an antenna positioned on a passing airplane, and the resulting Doppler spectrum will be obtained at various receiving angles.

Aside from SAR imaging, the work presented herein may have application to other areas of research. For example, the modeling results may aid the development of improved detection techniques for improvised explosive devices (IEDs) via electromagnetic wave interactions with a mechanically vibrating Earth. This is made possible by the fact that targets (IEDs) in a background medium (Earth) are more easily detected when the Earth (with targets) are vibrating, a

fact that could possibly help save countless lives. Analogously, the detection of early-stage breast cancer might be improved via vibrations [6].



## Chapter 2

### Background

#### 2.1 Modeling Moving Objects in FDTD Grids

Initially, researchers used a brute-force method to implement vibrations in their FDTD grids. For instance, in [7], Bircher et al. are interested in the rotor-blade modulation (RBM), which is an effect where the rotation of a helicopter's rotor blade periodically interferes with the aircraft communication by distorting the signals. In an FDTD grid, they utilized "a quasi-stationary" [8] method to model the rotor blade movement. This approach is accomplished by considering each orientation of the rotor blades as one instant of time. The plane radiation patterns are calculated using separate FDTD simulations for each of the rotor orientations. Then at each observation angle they compute the motor modulation by subtracting the resulting maximum and minimum electric field for every rotor orientation.

$$\text{modulation level} = 20 \text{Log}_{10}(|E_{max}| - |E_{min}|)$$

Several other articles introduce a boundary condition type method for modeling the effects of vibrations that includes rigorous calculations resulting in currents applied to the surface of the object [9-11]. However, the approach in [9] does not take into consideration arbitrary vibrations and the method in [10,11] does not pertain to objects with arbitrary geometry.

The authors of [10,11] realize the limitations of their method, as well as the limitations of the technique employed in [9]. Thus, they propose a time-varying sheet boundary condition (SBC), which is a more generalized version of the impedance boundary condition (IBC). The SBC is a boundary condition applied to the surface of an unperturbed object that represents any slight perturbation within or on the surface of the moving object. This boundary condition can be implemented for any arbitrary geometry and mode of vibration.

For objects that are vibrated acoustically, there is often a significant (orders of magnitude) difference between the acoustic frequency and EM frequency. Thus, the quasi-stationary (QS) approximation [8] is assumed for the SBC. The quasi-stationary approximation assumes that the scattered field is estimated to be stationary (with respect to the moving object) at any time, and as the time varies so does the scattered field calculation. The QS is only accurate when the EM frequency is much larger than the vibration frequency and when “the object is not moving at relativistic speeds” [12].

In a recent study [4], the SBC is applied to arbitrarily shaped objects in an FDTD grid to calculate the Doppler spectrum of the bistatic scattered field. In this Thesis, the methodology of the FDTD SBC [4] is employed to study the interaction of EM pulses with vibrating objects. Further details of the SBC and the implementation of the SBC are provided in the section 3.5.

## **2.2 Calculation of Diffraction Coefficients**

In [13], Stratis et al. look at diffraction coefficients of conducting and dielectric wedges. Their work is motivated by the fact that classical theories such as the

uniform geometrical theory of diffraction solve diffraction coefficient problems for perfect electrical conducting (PEC) wedges, but there is no analytical solution of the diffraction coefficient for problems that have dielectric or imperfectly conducting wedges. As a result, they utilize the full-vector Maxwell's equations FDTD method to numerically compute diffraction coefficients of dielectric and imperfectly conducting wedges. In this Thesis, this study is taken a step further and the FDTD method is employed to numerically calculate diffraction coefficients of dielectric and imperfectly conducting *vibrating* wedges.

## Chapter 3

### FDTD Model Components

#### 3.1 Introduction of FDTD

In a 1966 paper [1], K. S. Yee developed the basic FDTD space grid and time-stepping algorithm by taking the following Maxwell's equations and the equivalent set of finite difference equations

$$\frac{\partial \mathbf{B}}{\partial t} + \nabla \times \mathbf{E} = 0$$

$$\frac{\partial \mathbf{D}}{\partial t} - \nabla \times \mathbf{H} = \mathbf{J}$$

$$\mathbf{B} = \mu \mathbf{H}$$

$$\mathbf{D} = \epsilon \mathbf{E}$$

and put them into the following computational form

$$\begin{aligned} & \frac{B_x^{n+\frac{1}{2}}\left(i, j + \frac{1}{2}, k + \frac{1}{2}\right) - B_x^{n-\frac{1}{2}}\left(i, j + \frac{1}{2}, k + \frac{1}{2}\right)}{\Delta t} \\ &= \frac{E_y^n\left(i, j + \frac{1}{2}, k + 1\right) - E_y^n\left(i, j + \frac{1}{2}, k\right)}{\Delta z} \\ &- \frac{E_z^n\left(i, j + 1, k + \frac{1}{2}\right) - E_z^n\left(i, j, k + \frac{1}{2}\right)}{\Delta y} \end{aligned}$$

$$\begin{aligned}
& \frac{D_x^n \left( i + \frac{1}{2}, j, k \right) - D_x^{n-1} \left( i + \frac{1}{2}, j, k \right)}{\Delta t} \\
&= \frac{H_z^{n-1/2} \left( i + \frac{1}{2}, j + \frac{1}{2}, k \right) - H_z^{n-1/2} \left( i + \frac{1}{2}, j - \frac{1}{2}, k \right)}{\Delta y} \\
&- \frac{H_y^{n-1/2} \left( i + \frac{1}{2}, j, k + \frac{1}{2} \right) - H_y^{n-1/2} \left( i + \frac{1}{2}, j, k - \frac{1}{2} \right)}{\Delta z} + J_x^{n-1/2} \left( i + \frac{1}{2}, j, k \right)
\end{aligned}$$

Taflove further developed Yee's space grid and time-stepping algorithm and coined the term Finite-Difference Time-Domain and its corresponding acronym FDTD in a 1980 paper [14].

The programming methods in this Thesis were aided by Taflove and Hagness's textbook [2], which provides detailed explanations and programming details for FDTD. The basic 2-D TM<sub>z</sub> Maxwell's equations utilized in the code are

$$\nabla \times \vec{E} = -\mu \frac{\partial H}{\partial t} - \vec{M} \quad \longrightarrow \quad \frac{\partial E_z}{\partial t} = \frac{1}{\varepsilon} \left( \frac{\partial H_y}{\partial x} - \frac{\partial H_x}{\partial y} \right)$$

$$\frac{\partial H_y}{\partial t} = \frac{1}{\mu} \frac{\partial E_z}{\partial x}$$

$$\nabla \times \vec{H} = \varepsilon \frac{\partial E}{\partial t} + \vec{J} \quad \longrightarrow$$

$$\frac{\partial H_x}{\partial t} = -\frac{1}{\mu} \frac{\partial E_z}{\partial y}$$

Implementing central differencing and expanding these equations into the FDTD method yields

$$\frac{E_z|_{i,j}^{n+1} - E_z|_{i,j}^n}{\Delta t} = \frac{1}{\epsilon_{i,j}} \left( \frac{H_y|_{i+1/2,j}^{n+1/2} - H_y|_{i-1/2,j}^{n+1/2}}{\Delta x} - \frac{H_x|_{i,j+1/2}^{n+1/2} - H_x|_{i,j-1/2}^{n+1/2}}{\Delta y} \right)$$

$$\longrightarrow E_z|_{i,j}^{n+1} = E_z|_{i,j}^n + \frac{\Delta t}{\epsilon_{i,j}} \left( \frac{H_y|_{i+1/2,j}^{n+1/2} - H_y|_{i-1/2,j}^{n+1/2}}{\Delta x} - \frac{H_x|_{i,j+1/2}^{n+1/2} - H_x|_{i,j-1/2}^{n+1/2}}{\Delta y} \right)$$

$$\frac{H_x|_{i,j+1/2}^{n+1/2} - H_x|_{i,j+1/2}^{n-1/2}}{\Delta t} = -\frac{1}{\mu_{i,j+1/2}} \left( \frac{E_z|_{i,j+1}^n - E_z|_{i,j}^n}{\Delta y} \right)$$

$$\longrightarrow H_x|_{i,j+1/2}^{n+1/2} = H_x|_{i,j+1/2}^{n-1/2} - \frac{\Delta t}{\mu_{i,j+1/2}} \left( \frac{E_z|_{i,j+1}^n - E_z|_{i,j}^n}{\Delta y} \right)$$

$$\frac{H_y|_{i+1/2,j}^{n+1/2} - H_y|_{i+1/2,j}^{n-1/2}}{\Delta t} = \frac{1}{\mu_{i+1/2,j}} \left( \frac{E_z|_{i+1,j}^n - E_z|_{i,j}^n}{\Delta x} \right)$$

$$\longrightarrow H_y|_{i+1/2,j}^{n+1/2} = H_y|_{i+1/2,j}^{n-1/2} + \frac{\Delta t}{\mu_{i+1/2,j}} \left( \frac{E_z|_{i+1,j}^n - E_z|_{i,j}^n}{\Delta x} \right)$$

The H field update equations are first time stepped through, followed by the E field update equations. These equations are the basis of modeling the electromagnetic fields and wave propagation.

### 3.2 Introduction of TFSF

The Total-Field/Scattered-Field (TFSF) technique generates an incident plane wave that may propagate in any angular direction in the FDTD grid. To formulate the TFSF, the following equations are assumed:

$$E_{\text{total}} = E_{\text{inc}} + E_{\text{scat}} \qquad H_{\text{total}} = H_{\text{inc}} + H_{\text{scat}}$$

These equations state that the total fields are equal the sum of the incident fields plus the scattered fields. The  $E_{\text{inc}}$  and the  $H_{\text{inc}}$  are the E and H fields of an incoming uninterrupted wave.  $E_{\text{scat}}$  and  $H_{\text{scat}}$  are the E and H fields of a scattered wave due to the interaction of an incident wave with an object. To realize the TFSF, the total fields are modeled in region 1 as shown in the sample 2-D FDTD grid of Figure 1 and a zone of only scattered fields are modeled in region 2, which borders region 1.

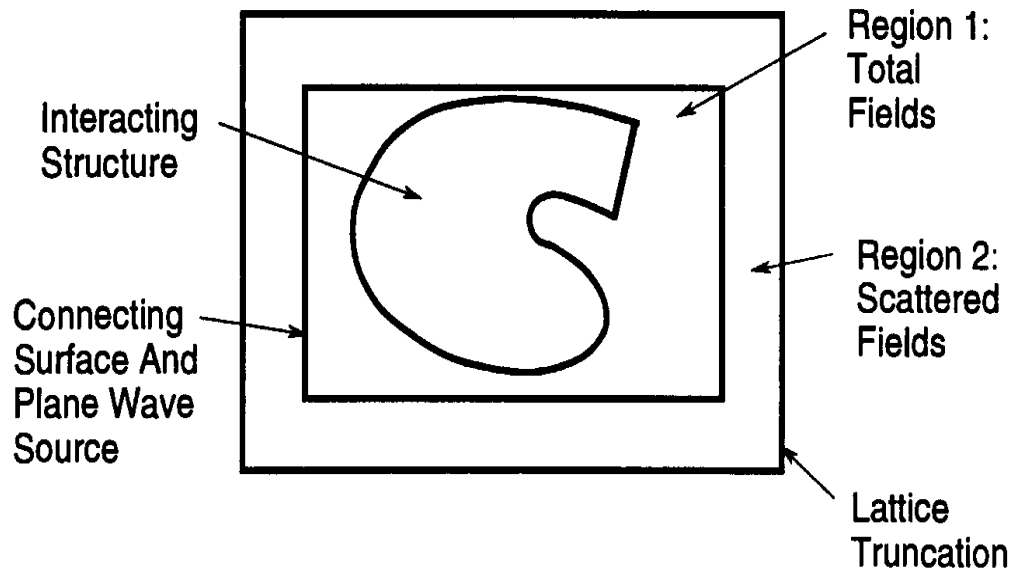


**Figure 1:** TFSF. A sample 2-D FDTD grid illustrating the two regions of modeled fields. Region 2, made up of scattered fields, surrounds region 1, which consists of total-fields. Courtesy of [6].

There are several advantages of zoning the total fields in one region and the scattered fields into another region. The first advantage is that the interface between these two regions generates an arbitrary incident wave in region 1. The incident plane wave generated can be modeled with any time waveform, duration, incident angle and polarization angle. Another advantage is that the continuity that occurs at the interface comes naturally between a total-field region and a scattered-field region and the programming of this interface is straightforward. Also advantageous is the ability to accurately compute EM fields in deep hidden regions. Additionally, an absorbing boundary condition (ABC) can be applied to the outer edge of the scattered-field only region. An ABC reduces any outward waves to almost negligible values, which makes the grid appear infinite. This topic will be discussed in the next section. The last advantage is that the far-field radiation or bistatic scattering pattern can be obtained by putting a near-to-far-field transformation surface in region 2, where there are only scattered-fields. This will be further discussed in section 3.4.

### **3.3 Introduction of Convolutional Perfectly Matched Layer (CPML)**

As mentioned previously, ABCs are implemented at the edge of an FDTD grid and terminate any unwanted reflections from the outer grid boundaries. Perfectly Matched Layer (PML) is a type of ABC, and it utilizes an outer-layer absorbing medium to reduce unwanted reflections. Figure 2 illustrates how the PML is introduced in an FDTD model. The PML is on the outer edges of this Figure, and it effectively introduces losses in each of the four directions of the grid. Once the wave, propagating in this case symmetrically outward, reaches the PML region the wave gets absorbed into the PML.



Convolutional PML [3] is a more recently developed and improved type of ABC, and it is the ABC implemented in this Thesis. CPML is the most accurate PML and is applicable for generalized material.

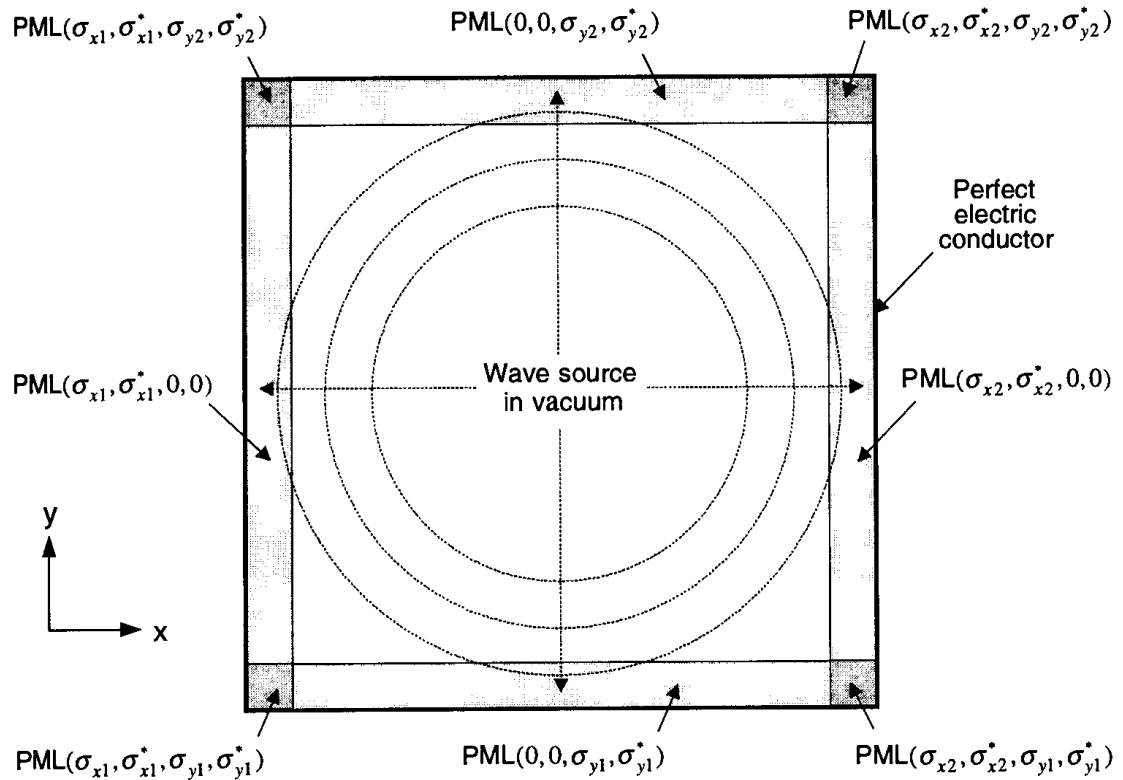


**Figure 2:** The PML is on the outer edges of this Figure, and it effectively introduces losses in each of the four directions of the grid. Courtesy of [6].

### 3.4 Introduction of the Frequency-Domain Near-to-Far-Field (NTFF) Transformation

The frequency-domain NTFF is computed by taking the transformation of the near-field data. The advantage of using this method is that the FDTD grid does not need to be extended out into the far-field in order to obtain far-field information. The 2-D  $TM_z$  scattering or radiation geometry utilized to attain the NTFF in the phasor domain is shown in Figure 3. In this Figure, is a structure enclosed by contour  $C_a$ . Surrounding both of these is the infinite-radius circular

contour  $C_\infty$ . With the assumption that  $C_a$  and  $C_\infty$  are connected, a continuous, closed contour is formed around the structure.

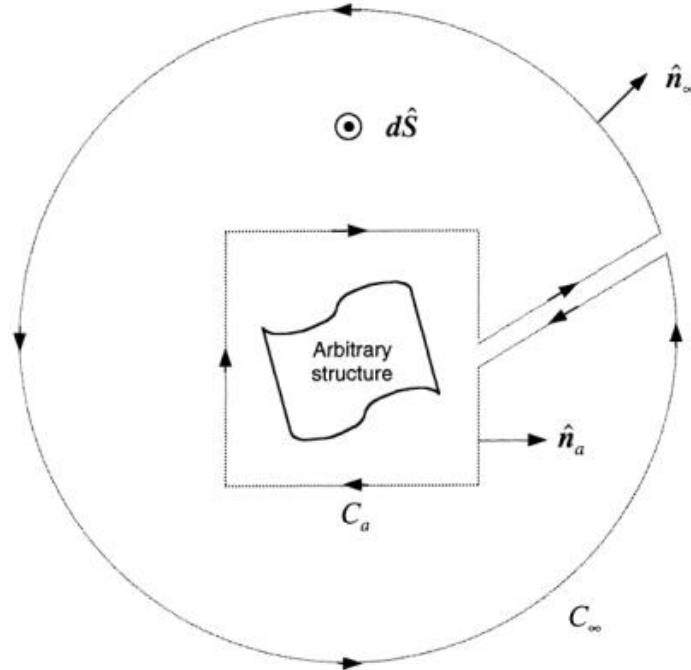


**Figure 3:** 2-D  $TM_z$  scattering or radiation geometry utilized to obtain the NTFF in the phasor domain. Courtesy of [6].

The first step in obtaining the NTFF in the frequency domain is to take the Discrete Fourier Transform (DFT) of the FDTD computed electric and magnetic fields utilizing the geometry in Figure 3. Then, apply Green's theorem to  $E_z(\mathbf{r})$  and  $G(\mathbf{r}|\mathbf{r}')$

$$\begin{aligned} & \int_S [\tilde{E}_z(\mathbf{r}')(\nabla^2)'G(\mathbf{r}|\mathbf{r}') - G(\mathbf{r}|\mathbf{r}')(\nabla^2)'\tilde{E}_z(\mathbf{r}')]ds' \\ &= \oint_{C_\infty} \left[ \tilde{E}_z(\mathbf{r}')\frac{\partial G(\mathbf{r}|\mathbf{r}')}{\partial r'} - G(\mathbf{r}|\mathbf{r}')\frac{\partial \tilde{E}_z(\mathbf{r}')}{\partial r'} \right] dC' - \oint_{C_a} \left[ \tilde{E}_z(\mathbf{r}')\frac{\partial G(\mathbf{r}|\mathbf{r}')}{\partial n_a'} \right. \\ & \quad \left. - G(\mathbf{r}|\mathbf{r}')\frac{\partial \tilde{E}_z(\mathbf{r}')}{\partial n_a'} \right] dC' \end{aligned}$$

With some math, this equation reduces to

$$\vec{E}_z(\mathbf{r}) = \oint_{C_a} [G(\mathbf{r}|\mathbf{r}') \hat{\mathbf{n}}_a' \cdot \nabla' \vec{E}_z(\mathbf{r}') - \vec{E}_z(\mathbf{r}') \hat{\mathbf{n}}_a' \cdot \nabla' G(\mathbf{r}|\mathbf{r}')] dC'$$

where  $\mathbf{r}$  is an observation point,  $\mathbf{r}'$  is a source point and  $dC'$  is a differential path along  $C_a$  and  $C_\infty$ .

Next, taking the limiting expression of the analytical form of the Green function

$$G(\mathbf{r}|\mathbf{r}') = \frac{j}{4} H_0^{(2)}(k|\mathbf{r} - \mathbf{r}'|)$$

$$\longrightarrow \lim_{k|\mathbf{r}-\mathbf{r}'| \rightarrow \infty} G(\mathbf{r}|\mathbf{r}') = \frac{j^{3/2}}{\sqrt{8\pi k}} \frac{e^{-jk|\mathbf{r}-\mathbf{r}'|}}{|\mathbf{r}-\mathbf{r}'|^{1/2}}$$

doing some arithmetic and plugging the final limiting expression of the analytical form of the Green function into the reduced  $\vec{E}_z(\mathbf{r})$  equation gives the far-field expression

$$\lim_{k|\mathbf{r}-\mathbf{r}'| \rightarrow \infty} \vec{E}_z(\mathbf{r}) = \frac{e^{j3\pi/4}}{\sqrt{8\pi k r}} e^{-jk r} \oint_{C_a} [\hat{\mathbf{n}}_a' \cdot \nabla' \vec{E}_z(\mathbf{r}') - jk \vec{E}_z(\mathbf{r}') \hat{\mathbf{n}}_a' \cdot \hat{\mathbf{r}}] e^{+jk \hat{\mathbf{r}} \cdot \mathbf{r}'} dC'$$

Then, manipulating the above equation results in the standard form

$$\lim_{k|\mathbf{r}-\mathbf{r}'| \rightarrow \infty} \vec{E}_z(\mathbf{r}) = \frac{e^{-jk r}}{\sqrt{r}} \frac{e^{j(\frac{\pi}{4})}}{\sqrt{8\pi k}} \oint_{C_a} \left[ \begin{array}{l} \omega \mu_o \hat{\mathbf{z}}' \cdot \vec{\mathbf{J}}_{eq}(\mathbf{r}') \\ -k \hat{\mathbf{z}}' \times \vec{\mathbf{M}}_{eq}(\mathbf{r}') \cdot \hat{\mathbf{r}} \end{array} \right] e^{+jk \hat{\mathbf{r}} \cdot \mathbf{r}'} dC'$$

where  $\vec{\mathbf{J}}_{eq} \equiv \hat{\mathbf{n}}_a \times \vec{\mathbf{H}}$  and  $\vec{\mathbf{M}}_{eq} \equiv -\hat{\mathbf{n}}_a \times \vec{\mathbf{E}}$  are the phasor tangential equivalent electric and magnetic currents at  $C_a$ .

### **3.5 Modeling Object Vibrations**

#### **3.5.1 Introduction of the Sheet Boundary Condition (SBC)**

Modeling the actual vibration of the object via brute-force methods in the FDTD model is difficult due to the fine resolution required to resolve the object's small vibration motion, the orders of magnitude difference between the scattering from the stationary object and the desired Doppler shifted scattered field component, and the large time scale difference between the electromagnetic signal and the object movement.

The sheet boundary condition (SBC), as mentioned in section 2.1, addresses these issues by acquiring only a single discretization of the object not determined by the magnitude of the vibrations, separating the dominant unperturbed scattering from the Doppler component due to the object motion, and accommodating the two time scales, electromagnetic and acoustic, without increasing the required computational resources. The SBC is applied on the unperturbed object boundary, and it accounts for any object motion or boundary deformation normal to the surface. Tangential (shear) boundary motion has a much smaller effect on the Doppler component and is thus not considered.

Specifically, the SBC analyzes the total scattered field, which is the combination of the electric fields scattered from the unperturbed object and the electric fields scattered from the vibrating object that contains some Doppler fields.

#### **3.5.2 Formulation**

The radial displacement,  $u_\rho(\phi, t)$ , which may change cosinusoidally, can be taken into consideration when modeling vibration of an object

$$u_p(\phi, t) = \sum_{n=0}^{\infty} \Gamma_n \cos(\omega_a t + \theta_n) \cos(n\phi) = \sum_{n=0}^{\infty} \delta_n(\phi, t)$$

where  $n$  is the mode number,  $\Gamma_n$  is the mode amplitude,  $\theta_n$  is the mode phase,  $\omega_a$  is the acoustic frequency and  $\phi$  is the azimuthal angle. In this Thesis the cosinusoidal time dependence is suppressed due to choosing a specific mode of vibration that is associated with a particular boundary perturbation. Thus, the equation utilized for the boundary perturbation is

$$\delta_n(\phi) = \Gamma_n \cos(n\phi)$$

In order to implement the SBC, two codes with the same parameters are created. In the first code, an incident plane wave source is employed and a stationary dielectric object is modeled within this grid. The electric fields along the boundary of the dielectric object are recorded versus time step. The second code is simulated with the only source being the currents along the boundary of the dielectric, which generate the Doppler component of the scattered field. The currents along the boundary for a dielectric object and  $TM_z$  polarization are modeled with

$$J_z = \hat{n} \times \hat{n} \times \left[ \delta(\vec{r}, \tau_i) (\varepsilon_2 - \varepsilon_1) \frac{\partial E}{\partial t} + \frac{\partial}{\partial s} \left( \delta(\vec{r}, \tau_i) \left( \frac{1}{\mu_1} - \frac{1}{\mu_2} \right) \int \frac{\partial E}{\partial s} dt \right) \right]$$

However, since the permeability in this study is 1, the above equation reduces to

$$J_z = \hat{n} \times \hat{n} \times \left[ \delta(\vec{r}, \tau_i) (\varepsilon_2 - \varepsilon_1) \frac{\partial E}{\partial t} \right]$$

where  $\delta(\vec{r}, \tau_i)$  is the boundary perturbation and  $E$  is where the recorded electric fields from the first code are implemented.

### 3.5.3 Validation Study

In order to implement the SBC, two codes are created. The first code models a 281 x 281 grid where  $dx=dy= 0.6$  mm,  $dt = 1.39$  ps and the number of time steps is 10,000. This grid contains the TFSF formulation, CPML boundary condition and the NTFF transformation. The source is a Gaussian modulating a sinusoid at 5 GHz center frequency. A square cylinder with a width and length of  $2.0\lambda$ , a relative permittivity of 2 and a relative permeability of 1 is located in the middle of a free space FDTD grid. In this code, electric fields along the boundary of the unperturbed square cylinder are recorded versus time step.

In the second code, the electric field outputs from code 1 are used as currents along the boundary of the square cylinder that serves as the source to generate the Doppler component of the scattered field. The equation for the currents is given by

$$J_s = \hat{n} \times \hat{n} \times \left[ \delta(\vec{r}, \tau_i) (\epsilon_2 - \epsilon_1) \frac{\partial E}{\partial t} \right]$$

which is the equation utilized as the source in code 2.

The specific boundary perturbation chosen for this validation study is mode 2 and implemented by the following equation

$$\delta_2 = 0.01\lambda_o \cos(2\phi)$$

The mode amplitude,  $\Gamma$ , is  $0.001\lambda_o$  and  $\phi$  is computed by the angle around the cylinder. Figure 4 illustrates some of the mentioned parameters of the square dielectric.

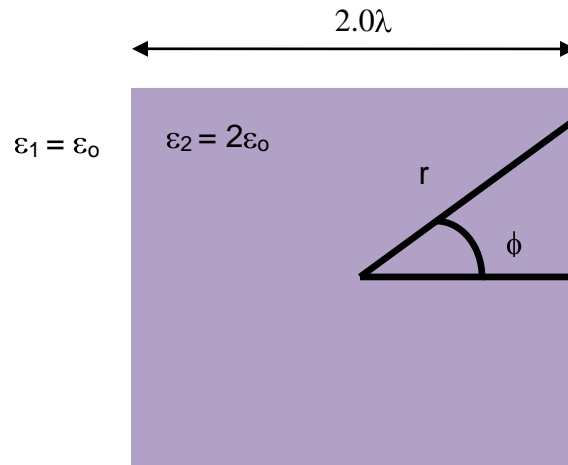


**Figure 4:** A square cylinder with a width and length of  $2.0\lambda$ , a relative permittivity of 2 and an azimuthal angle denoted by  $\phi$  located in the middle of a free space FDTD grid.

All of the parameters chosen are the same as the parameters used in [4] in order to compare the results obtained from [4] with the code for this Thesis.

Section 3.5.4 below provides the results of the validation study. Using a side by side comparison, the results attained from the model in this Thesis and the results from [4] seem to have good agreement. However, a brute-force method is also applied in order to fully verify that the SBC in this code is providing accurate results.

In order to carry out this brute-force technique, first, a set of two codes implementing the SBC simulate a square dielectric with a width and length of  $1.0\lambda$  and a relative permittivity of 2, which is located in the center of a  $281 \times 281$  grid. The source is a Gaussian modulating a sinusoid with a center frequency of 850 MHz and a Gaussian envelope of 1.3 ns duration (full width at half maximum). The number of time steps is 10,000,  $dx=dy= 3.53$  mm,  $dt = 8.15$  ps,

the incident angle is  $0^\circ$  and the amplitude vibration is 7 mm in the horizontal direction, along the x-axis. From this code the RCS is computed.

Second, a set of two codes without the SBC is set to have the same grid and object parameters as the above codes having the SBC. The only difference is that in this set of two codes there is an incident plane wave source and a stationary dielectric object in the center of the grid. The first simulation of this set of codes is run and the electric fields in the far-field are computed and recorded. Next, the left and right side of the object in this code are both moved outward 7 mm, to represent the vibration movement. This code is run again with the new object modification, and the electric fields in the far-field in this simulation are subtracted from the electric fields in the far-fields from the previous simulation with the object in the initial position. The RCS of the difference of these electric fields is computed. Finally, the RCS obtained from the code with the SBC is compared to the RCS of the brute-force method, which is presented in the results section. Note, the grid cell resolution was set to  $\lambda_0/100$  for accuracy, and in order to finely resolve a 7 mm movement in the code without the SBC.

#### **3.5.4 Validation Study Results**

After simulating the same parameters for the square cylinder in [4], the results obtained for this Thesis appeared to match very well with the results from [4] with a simple side by side comparison. This is shown in Figures 5 and 6 below.



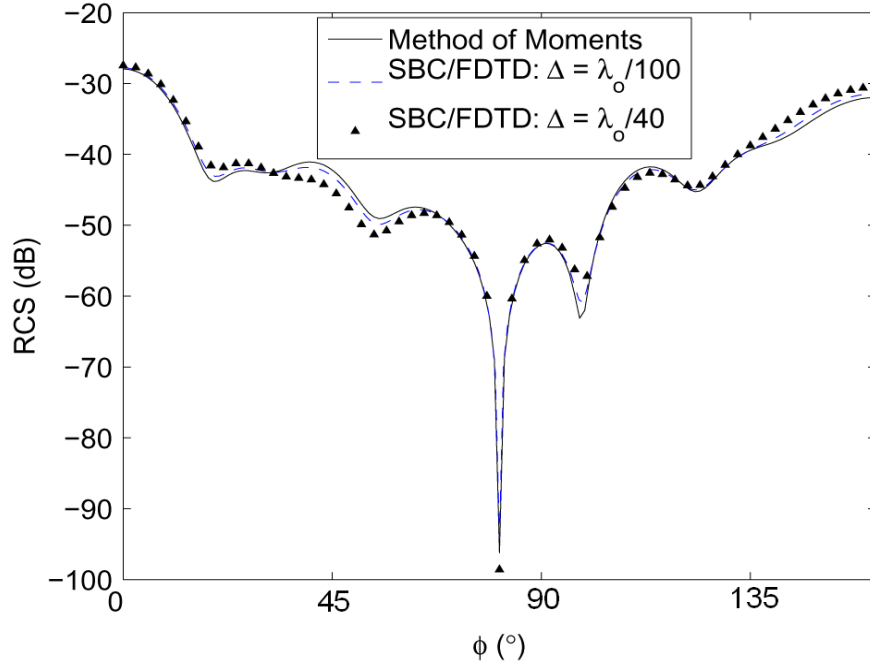


**Figure 5:** Results obtained from [1] for the RCS of a square cylinder with a width and length of  $2.0\lambda$ , a relative permittivity of 2, an azimuthal angle denoted by  $\phi$  and at an incident angle of  $0^\circ$ . Courtesy of [4].

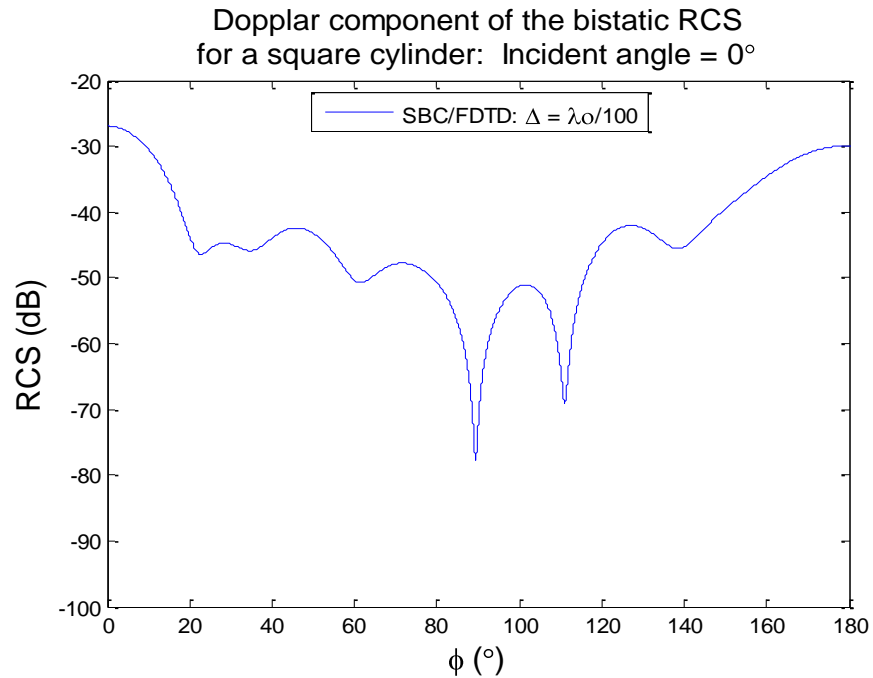


**Figure 6:** Results obtained from the code in this thesis for the RCS of a square cylinder with a width and length of  $2.0\lambda$ , a relative permittivity of 2, an azimuthal angle denoted by  $\phi$  and at an incident angle of  $0^\circ$ .

Using the parameters in [4], the RCS for various incident angles of a plane wave impinging on a square dielectric are also analyzed. Three randomly chosen incident angles,  $30^\circ$  (Figure 7),  $60^\circ$  (Figure 8) and  $90^\circ$  (Figure 9) are displayed to show the various signatures that can be obtained. Considering the overall goals for the work of this Thesis discussed in Chapter 1, it is important to analyze and recognize signatures from various incident angles, since the incident plane wave originating from a moving aircraft will be coming in at various angles.

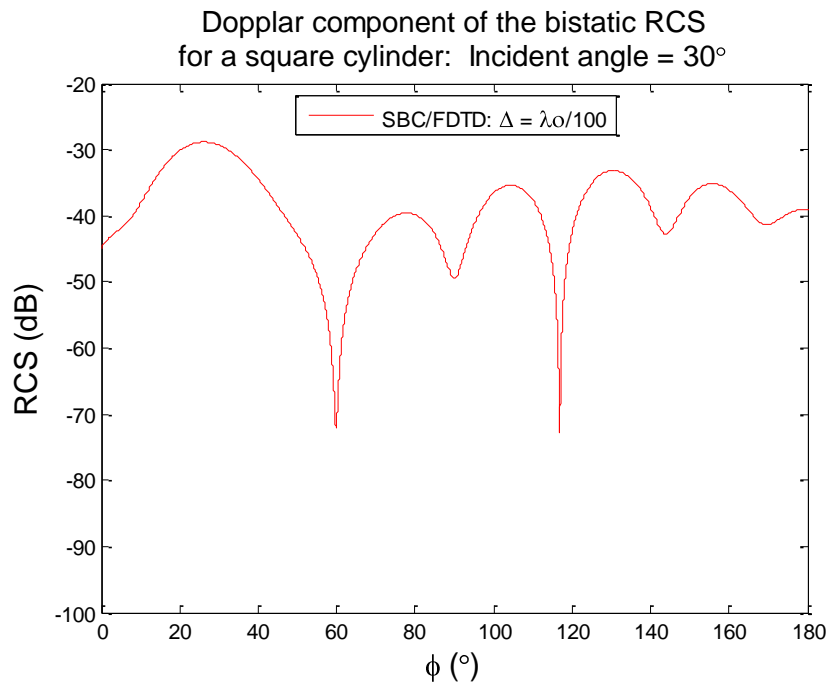


**Figure 7:** RCS of a square cylinder with a width and length of  $2.0\lambda$ , a relative permittivity of 2, an azimuthal angle denoted by  $\phi$  and at an incident angle of  $30^\circ$ .

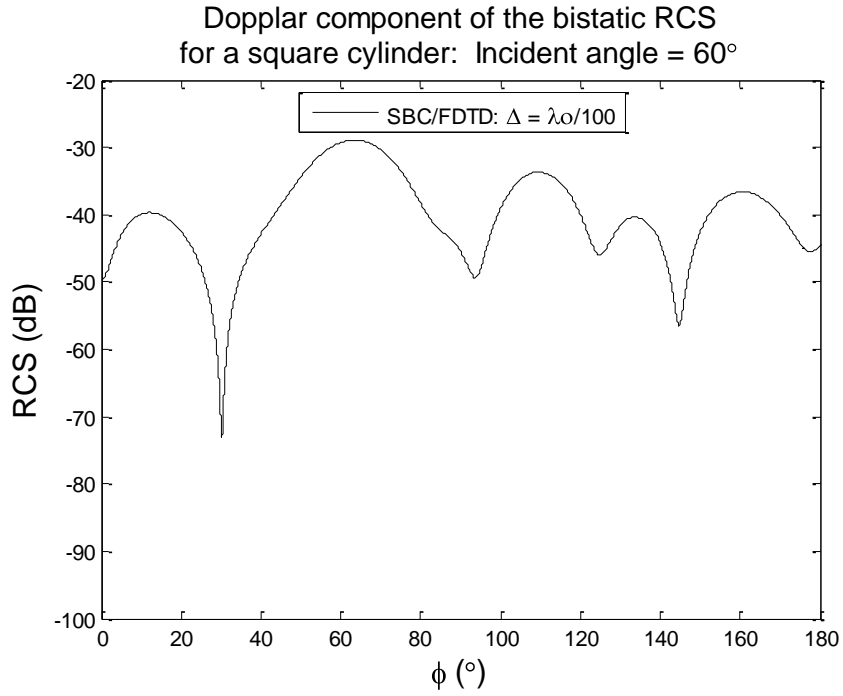


**Figure 8:** RCS of a square cylinder with a width and length of  $2.0\lambda$ , a relative permittivity of 2, an azimuthal angle denoted by  $\phi$  and at an incident angle of  $60^\circ$ .

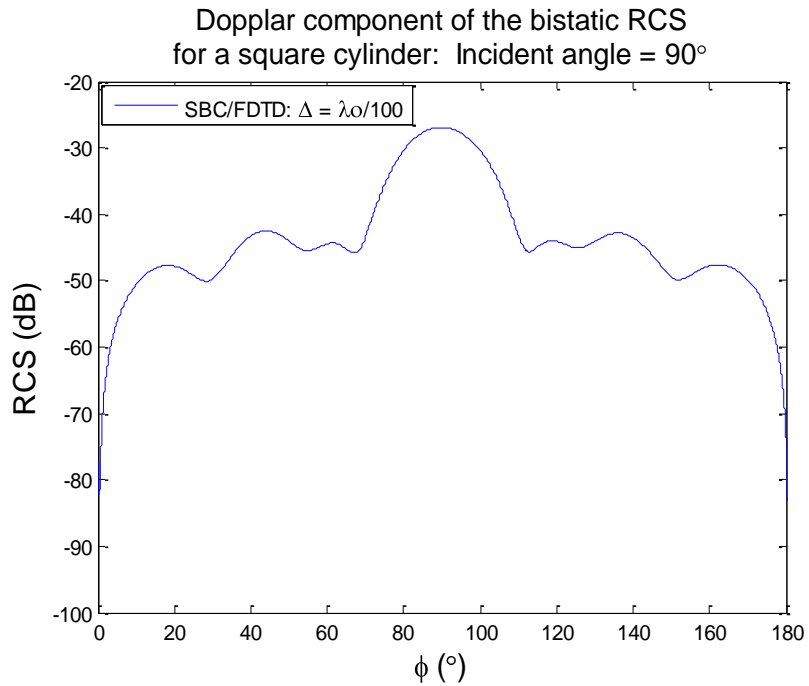


**Figure 9:** RCS of a square cylinder with a width and length of  $2.0\lambda$ , a relative permittivity of 2, an azimuthal angle denoted by  $\phi$  and at an incident angle of  $90^\circ$ .

Secondly, as mentioned in the previous Section, a brute-force modeling methodology was implemented in order to completely verify that the SBC is functioning correctly for the vibrations considered later in this Thesis. A comparison between the results of the RCS of the code with the SBC to the results of the RCS of the brute-force method is presented in Figure 10.

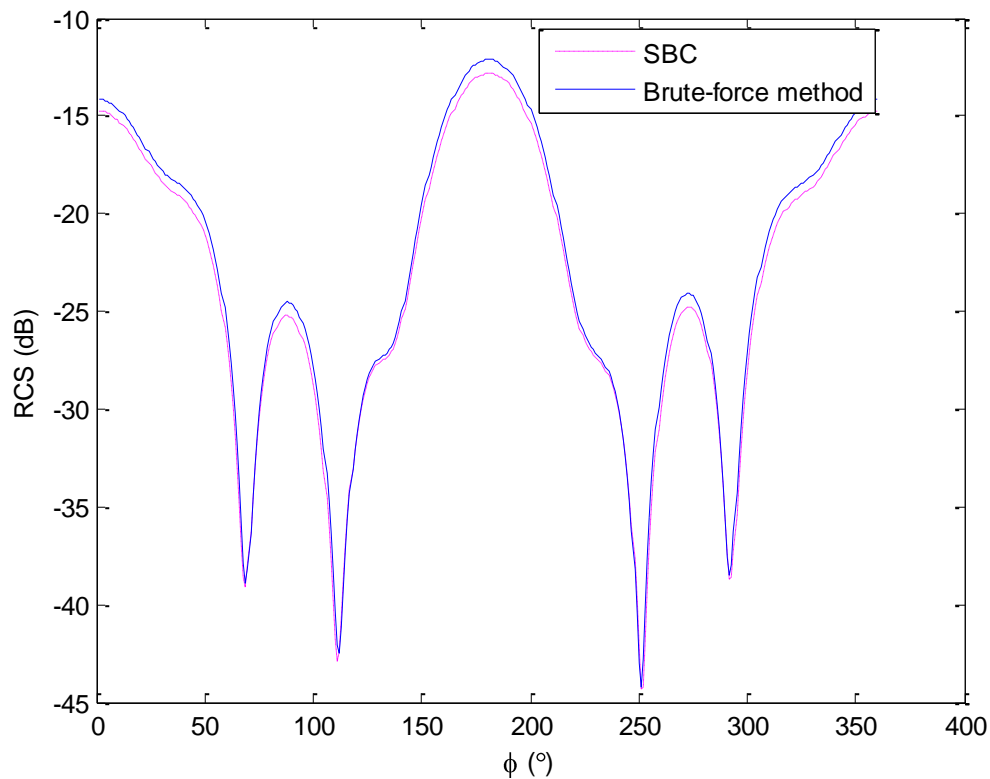


**Figure 10:** Comparison between the SBC vibrating at 7 mm and the brute-force method of physically moving an object 7 mm.

### 3.6 Calculation of the Diffraction Coefficient

#### 3.6.1 Methodology

In order to study diffraction coefficients, the authors in [13] implement time-gating, which allows for the separation of the incident, reflected, near-edge

diffracted and far-edge diffracted waveforms. The purpose of utilizing this technique is such that only the diffracted fields from the intended edge may be extracted from the FDTD grid in a straightforward manner to calculate the diffracted impulse response,  $h_{num}(\rho, \phi, t)$ .

Taking the Fourier transform of the diffracted impulse response,  $H_{num}(\rho, \phi, \omega)$  provides the variation of the diffracted field from a plane wave over a large frequency spectrum. The diffraction coefficient,  $D_{num}$ , is then obtained by the following equation

$$D_{num}(\rho, \phi, \omega) = H_{num}(\rho, \phi, \omega) \sqrt{r} e^{j\beta r}$$

where  $(\rho, \phi)$  is the observation point and  $r$  is the distance from the scattering edge to the observation point.

### 3.6.2 Validation Study

In order to verify the methodology for obtaining the diffraction coefficients, the validation study as performed in [13] for the case of a PEC right-angle wedge is performed. The FDTD-calculated results are then compared to the analytical solutions obtained via the uniform geometrical theory of diffraction (UTD).

The implemented 2-D  $TM_z$  polarized model has a grid size of 1,656 x 1,656, which includes a PML of 10 grid cells on all four sides, with a square PEC of 800 x 800. The bottom of the square PEC is located 728 grid cells from the bottom of the grid and the right side of the square PEC is located 728 grid cells from the right side of the grid. The source is a Gaussian modulating a sinusoid with a center frequency of 850 MHz and a Gaussian envelope of 1.3 ns duration (full width at half maximum). The number of time steps is 4,906,  $dx=dy= 8.82$  mm and

dt is 20.38 ps. The incident angle is  $80^\circ$  and the observation point, denoted by Point F in Figure 11, is located slightly to the right of the square PEC at  $\rho=6.3$  and  $\phi=262.37^\circ$ , in the diffracted field only region. The edge yielding the diffracted waves considered in this study is located at the bottom-right of the square PEC (a  $90^\circ$  wedge angle), edge A. The distance from the scattering edge to the observation point is represented with  $\rho$ , and the angle from the scattering edge to the observation point is denoted with  $\phi$ . These parameters can be referenced in Figure 11.

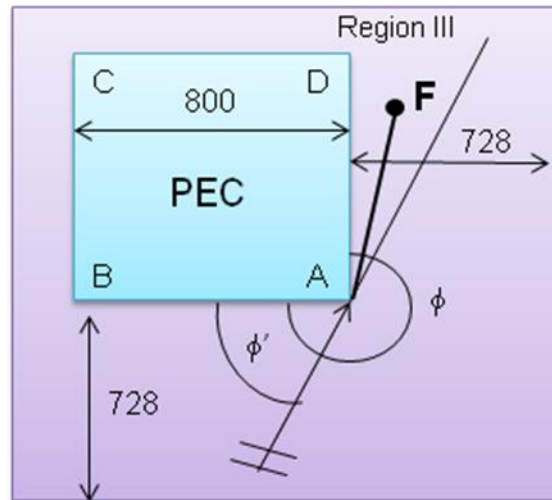


**Figure 11:** Parameters of the FDTD Grid that computes the Diffraction Coefficient at Point F.

In order to obtain the diffraction coefficient, the Fourier transform is taken of the electric fields at the observation point, F, and normalized relative to the incident plane wave source

$$H_{num}(\rho, \phi, \omega) = \frac{\mathcal{F}\{X_{dif}(\rho, \phi, t)\}}{\mathcal{F}\{X_{inc}(0, \phi, t)\}}$$

and utilizing the previously described  $D_{num}$  equation, the diffraction coefficient is computed by

$$D_{num}(\rho, \phi, \omega) = H_{num}(\rho, \phi, \omega) \sqrt{r} e^{j\beta r} = \frac{\mathcal{F}\{X_{dif}(\rho, \phi, t)\}}{\mathcal{F}\{X_{inc}(0, \phi, t)\}} \sqrt{\rho} e^{j\beta \rho}$$

Note that Point F is in the shadow scattering region, which is of practical interest for diffraction problems.

To obtain the UTD analytical solution, the computer code provided in [15] is utilized. This computer code computes the diffraction coefficient using the equation

$$\begin{aligned} D_s(\rho, \phi, \phi', \omega) &= \frac{-e^{-j\pi/4}}{2n\sqrt{2\pi\beta}} \left[ \left( \cot\left(\frac{\pi + \xi^-}{2n}\right) F(\beta, \rho, g^+(\xi^-)) \right. \right. \\ &\quad \left. \left. + \cot\left(\frac{\pi - \xi^-}{2n}\right) F(\beta, \rho, g^-(\xi^-)) \right) \right. \\ &\quad \left. - \left( \cot\left(\frac{\pi + \xi^+}{2n}\right) F(\beta, \rho, g^+(\xi^+)) + \cot\left(\frac{\pi - \xi^+}{2n}\right) F(\beta, \rho, g^-(\xi^+)) \right) \right] \end{aligned}$$

where  $\xi^+ = \phi + \phi'$ ,  $\xi^- = \phi - \phi'$ ,  $n$  is the wedge factor which is 1.5 for a right angle wedge and  $F(X)$  is the Fresnel's transition function computed by the asymptotic expressions for large and small arguments

$$F(X) \approx \left( \sqrt{\pi X} - 2Xe^{j\pi/4} - \frac{2}{3}X^2 e^{-j\pi/4} \right) e^{j\left(\frac{\pi}{4} + X\right)}$$

(for  $X < 0.3$ )

$$F(X) \approx 1 + j\frac{1}{2X} - \frac{3}{4X^2} - j\frac{15}{8X^3} + \frac{75}{16X^4}$$

(for  $X > 5.5$ ).

### 3.6.3 Validation Study Results

In Figures 12-15, visualizations that depict four snapshots of the behavior of the electric fields in the FDTD grid used for the validation study are provided. That is, the incoming plane wave at  $80^\circ$  is observed, as well as how the fields scatter and diffract once this plane wave interacts with the square PEC object, in particular around corner A of the PEC object, located in the upper left side of the grid. In these Figures, the black square superimposed on the image shows the location of the scatterer and A denotes the corner of interest.

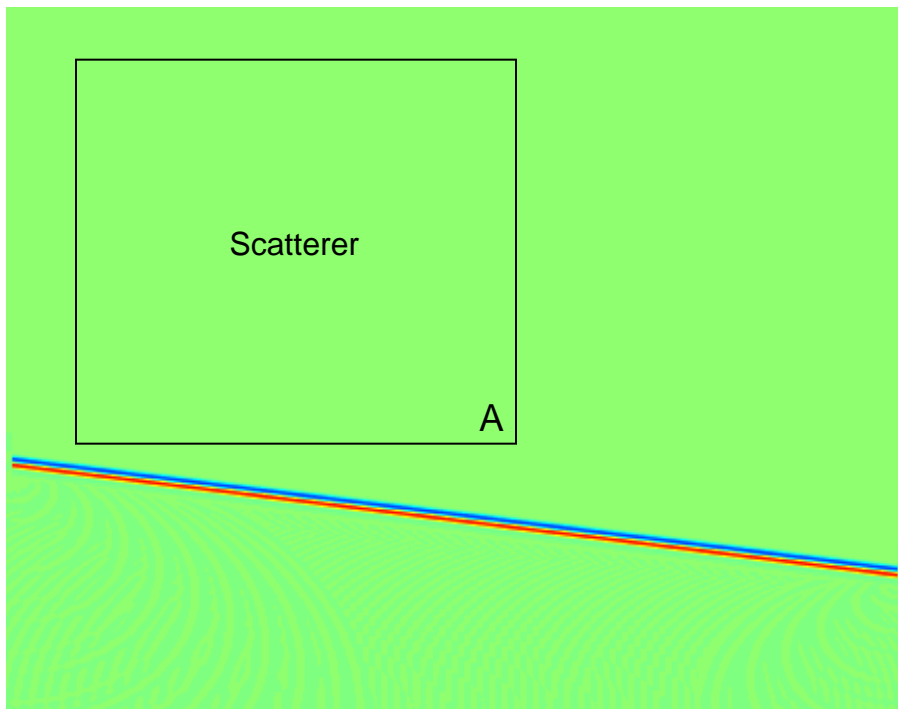


**Figure 12:** Snapshot at time step 1,000 of an incoming plane wave at  $80^\circ$  propagating towards a square PEC object located at the upper left of the grid.



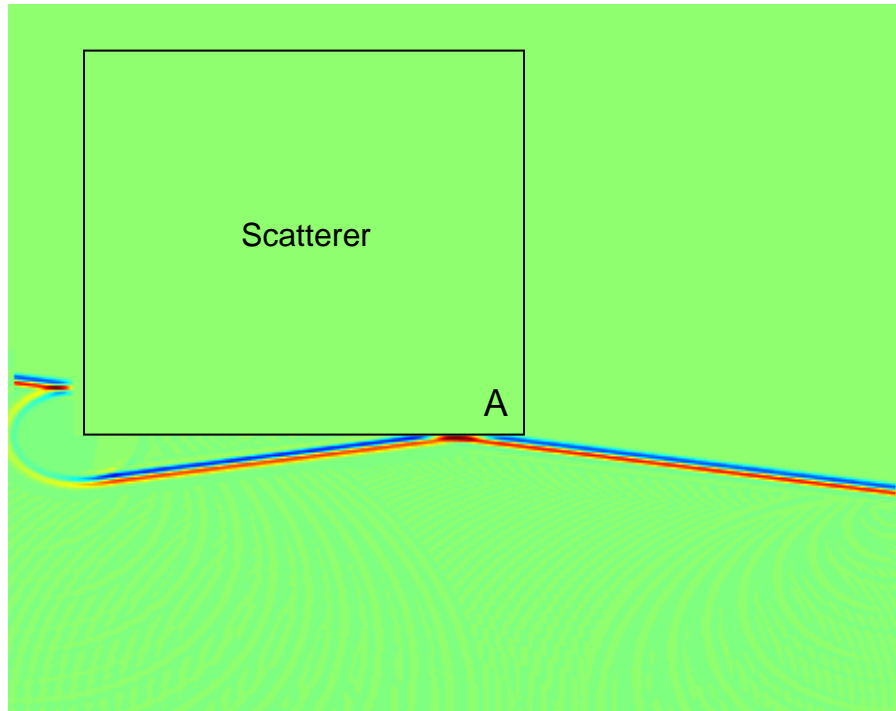


**Figure 13:** Snapshot at time step 1,300 of the scattering and diffracting of the electric fields once an incoming plane wave at  $80^\circ$  interacts with a square PEC object located at the upper left of the grid, and in particular corner A of the PEC object.

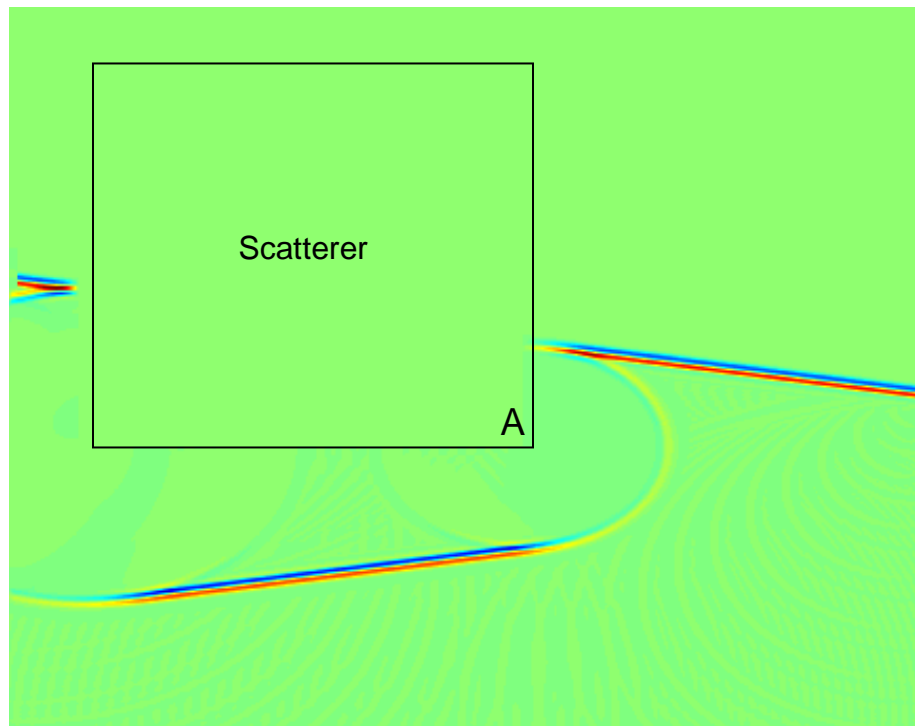


**Figure 14:** Snapshot at time step 1,700 of the scattering and diffracting of the electric fields once an incoming plane wave at  $80^\circ$  interacts with a square PEC object located at the upper left of the grid, and in particular corner A of the PEC object.

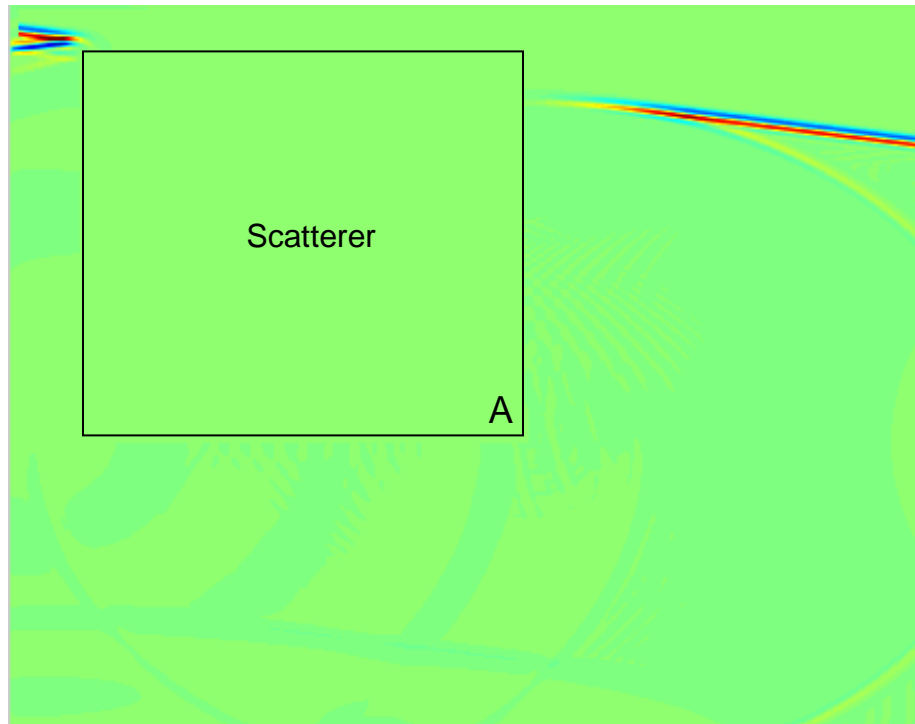


**Figure 15:** Snapshot at time step 2,600 of the scattering and diffracting of the electric fields once an incoming plane wave at  $80^{\circ}$  interacts with a square PEC object located at the upper left of the grid, and in particular corner A of the PEC object.

As mentioned previously, UTD analytical solutions for the diffraction coefficient are obtained to verify the methodology for obtaining the diffraction coefficient in this Thesis. As displayed in Figure 16, there is very good agreement between both the results of the analytical solutions and the FDTD simulated results. Specifically, as shown in Figure 17, the relative error is less than 1% from ~50 MHz to 1500 MHz. These results demonstrate the good degree of accuracy of the FDTD code utilized to compute the diffraction coefficient.

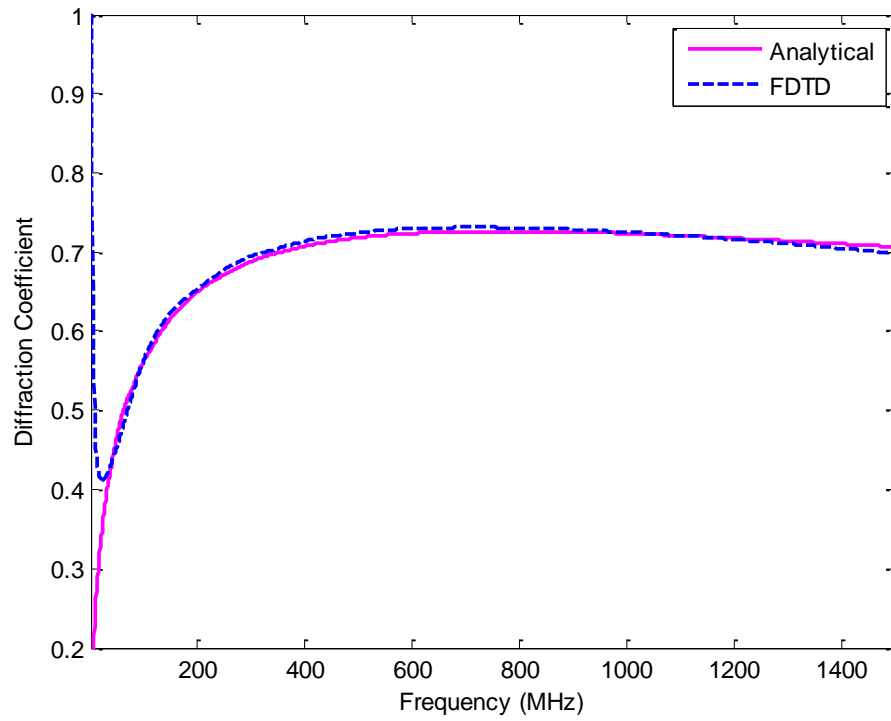


**Figure 16:** Comparison between the Analytical Solution and the FDTD results for the diffraction coefficient for a PEC object at Point F ( $\rho=6.3$ ,  $\phi=262.37^\circ$ )

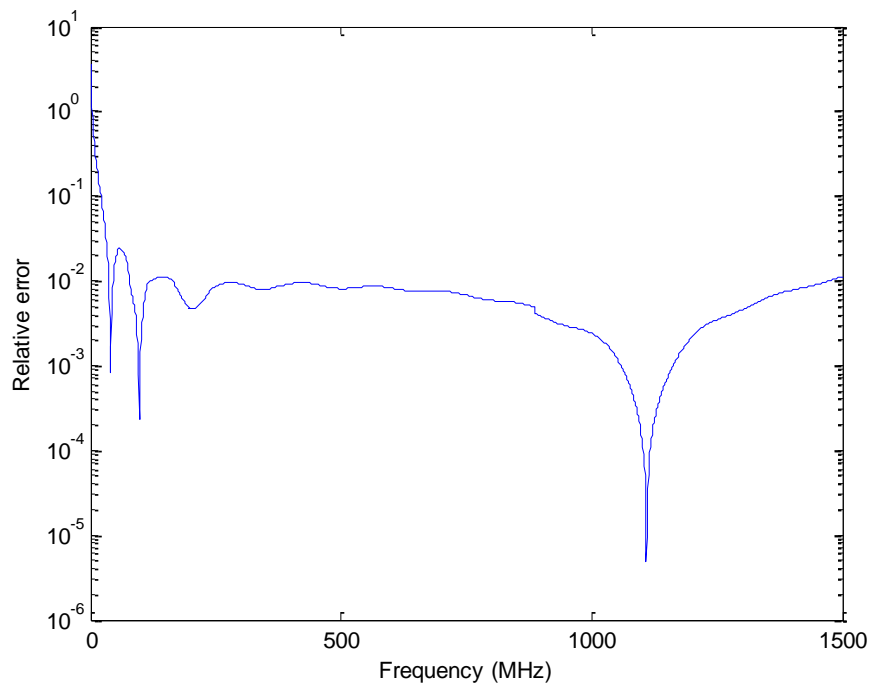


**Figure 17:** Relative Error between the analytical and FDTD results of the diffraction coefficient.

## Chapter 4

### Modeling Studies and Results

In this Chapter, the methodologies verified in Chapter 3 for modeling vibrating objects (utilizing SBC) and for calculating diffraction coefficients are combined to yield calculations of diffraction coefficients of vibrating wedges. Obtaining such results via analytical analyses is not viable. Diffraction coefficients for stationary dielectric and lossy objects (also not feasible to obtain via analytical analyses) are also provided for comparison.

The results herein are obtained by maintaining the same exact parameters and method for the PEC but changing the square PEC object to a vibrating lossless or lossy dielectric square object. The chosen conductivity and permittivity values are taken from [13]. The lossless dielectric is modeled with a relative permittivity of 2, 5 and 7 and the lossy dielectric is modeled with a fixed relative permittivity of 7 and conductivity of 10.

Each of these values are simulated with the object vibrating vertically, along the y-axis, or horizontally, along the x-axis with an amplitude of 5 mm

To include the finite conductivity in the vibrations, the following equation is utilized for the SBC

$$J_{z\delta}^a = - \left[ \delta(\varepsilon_2 - \varepsilon_1) \frac{\partial E_{oz}}{\partial t} \Big|_{n-\frac{1}{2}} + \delta(\sigma_2 - \sigma_1) E_{oz} \Big|_{n-\frac{1}{2}} \right]$$

Finally, note that for the chosen plane wave illumination angle (80°) and for the dielectric object material parameters, the refracted wave from face AD of the wedge undergoes total internal reflection.

#### 4.1 Diffraction Coefficients of Lossless Dielectric Wedges

A similar visualization as in Figures 12-15 is repeated in Figures 18-21, but this time depicting the scattering and diffracting of the electric fields once an incoming plane wave at  $80^\circ$  interacts with corner A of a square lossless dielectric object with a relative permittivity of 7, located at the upper left of the grid.

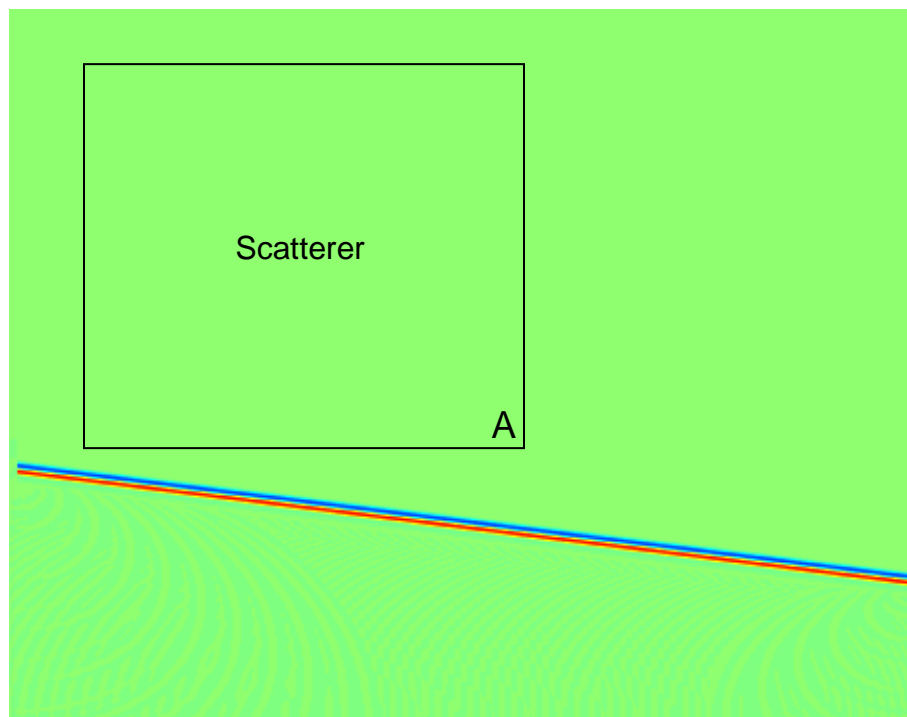


**Figure 18:** Snapshot at time step 1,000 of an incoming plane wave at  $80^\circ$  propagating towards a square dielectric object located at the upper left of the grid.

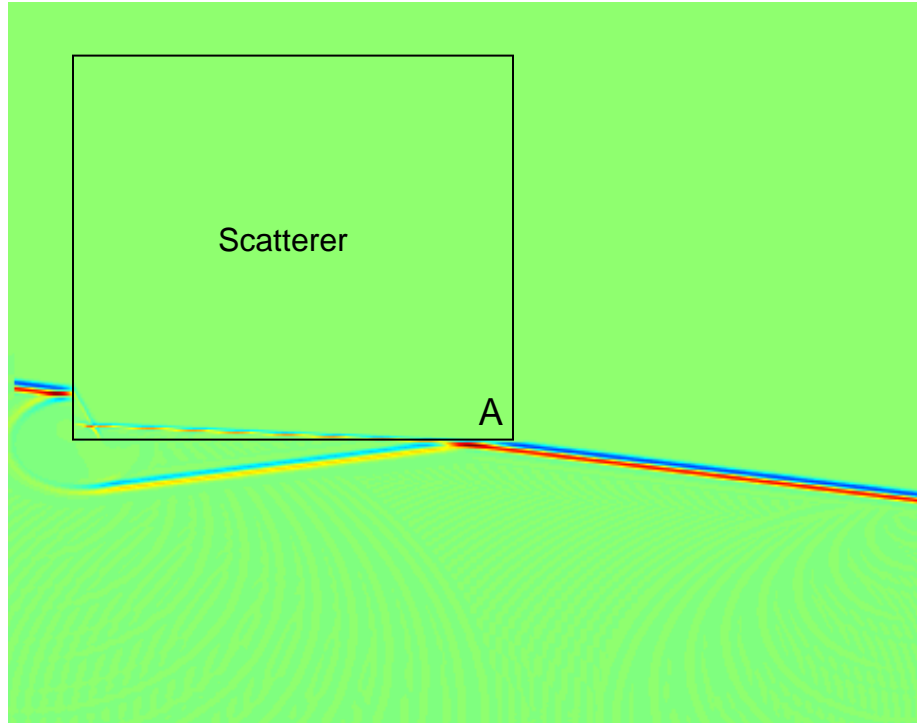


**Figure 19:** Snapshot at time step 1,300 of the scattering and diffracting of the electric fields once an incoming plane wave at  $80^\circ$  interacts with a square dielectric object located at the upper left of the grid, and in particular corner A of the dielectric object.

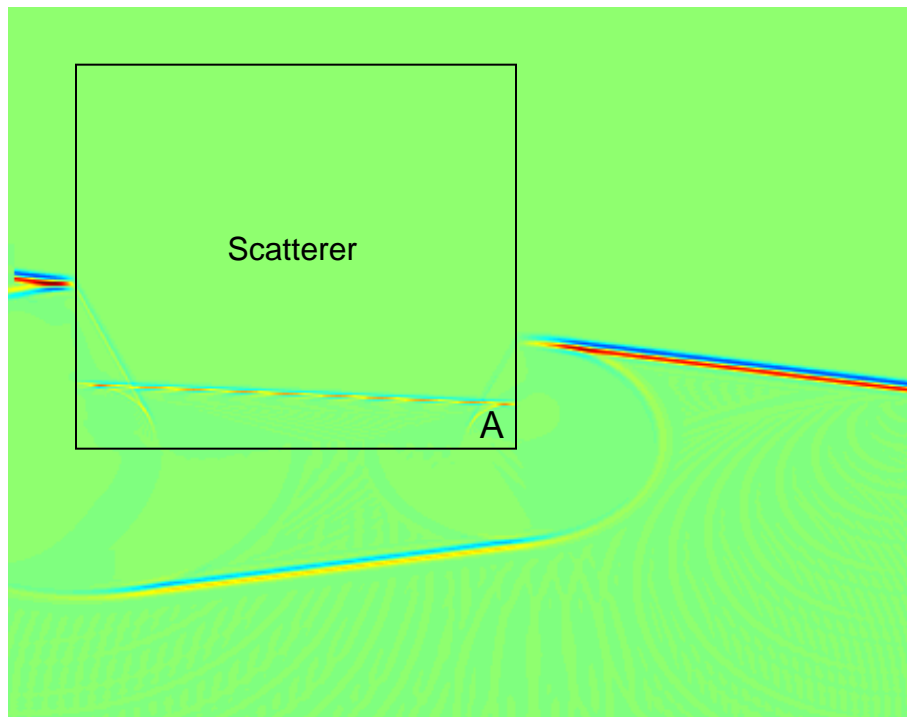


**Figure 20:** Snapshot at time step 1,700 of the scattering and diffracting of the electric fields once an incoming plane wave at  $80^\circ$  interacts with a square dielectric object located at the upper left of the grid, and in particular corner A of the dielectric object.

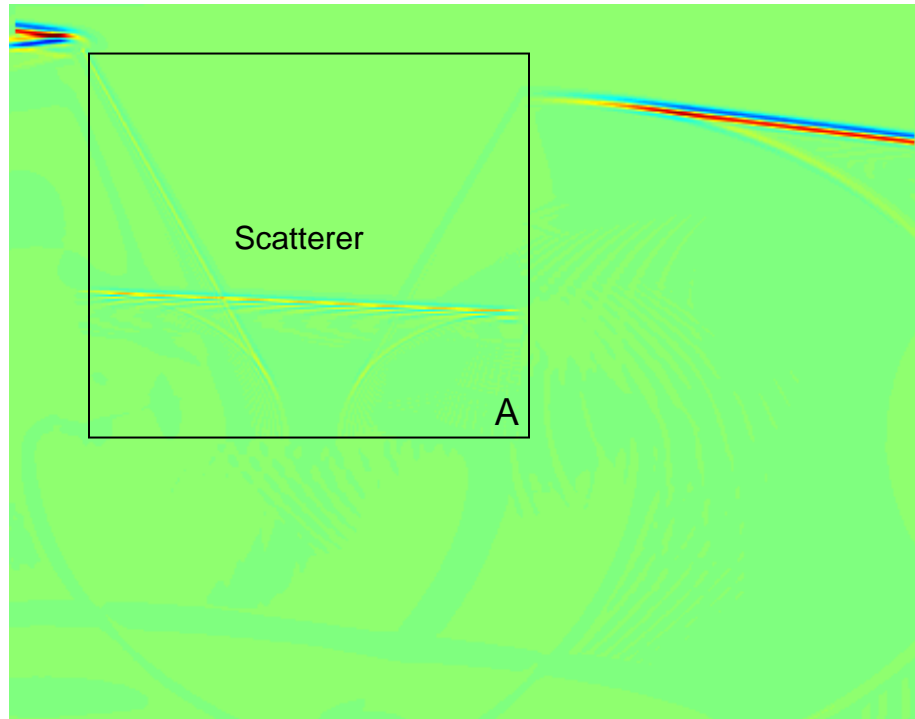


**Figure 21:** Snapshot at time step 2,600 of the scattering and diffracting of the electric fields once an incoming plane wave at  $80^\circ$  interacts with a square dielectric object located at the upper left of the grid, and in particular corner A of the dielectric object.

#### 4.1.1 Stationary Dielectric Wedges

Figure 22 shows the comparison between the diffraction coefficients of stationary lossless square dielectric objects having a relative permittivity of 2, 5 and 7.

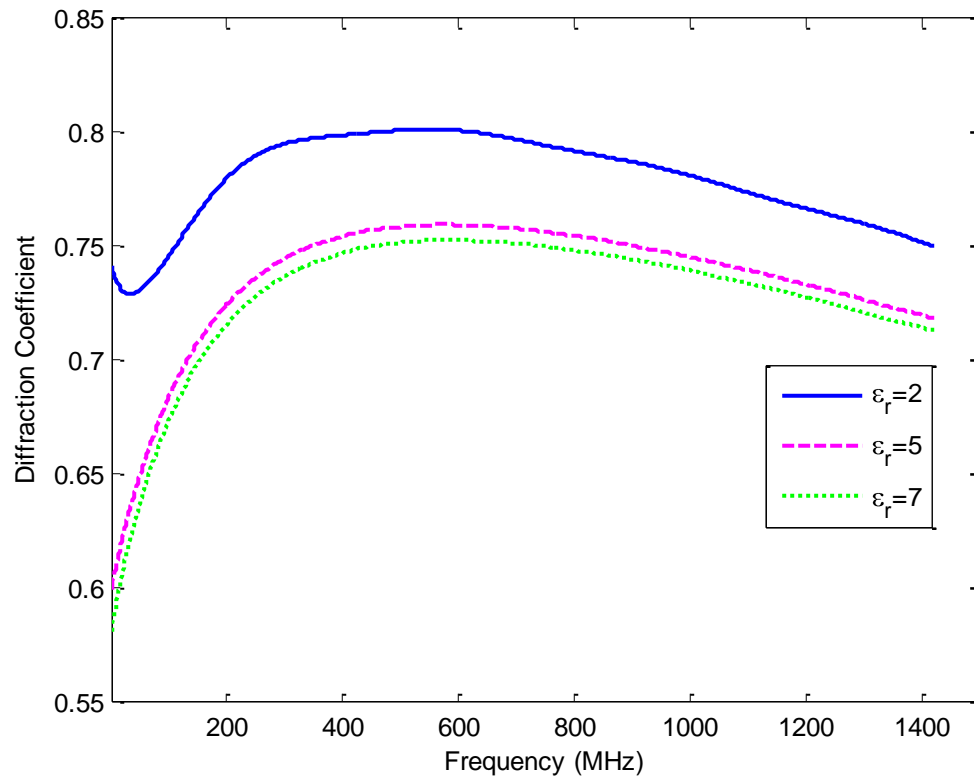


**Figure 22:** Comparison between the diffraction coefficients for a lossless stationary square dielectric object with a relative permittivity of 2, 5 and 7.

#### 4.1.2 Vertically (along the y-axis) Vibrating Dielectric Wedges

Analyzing the affects that a vibrating object has on the diffraction coefficient, the variation of the magnitude of the Doppler diffraction coefficients for lossless square dielectric objects vibrating vertically, along the y-axis, with a relative permittivity of 2, 5 and 7 are displayed in Figure 23.



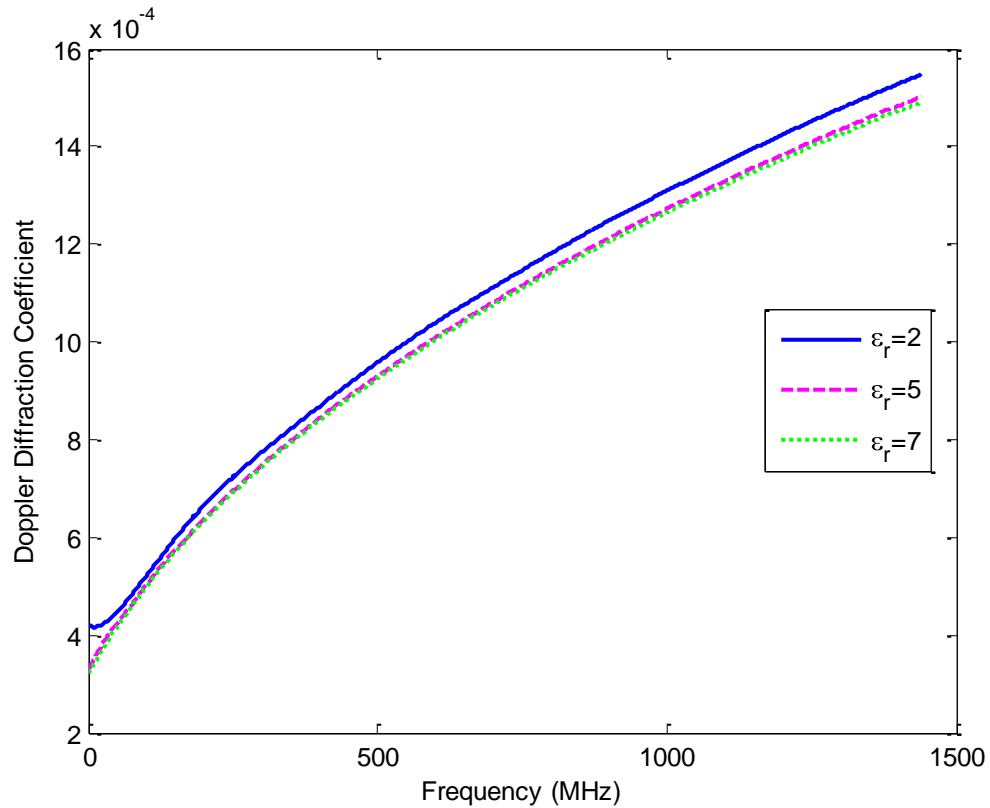


**Figure 23:** Comparison between the Doppler diffraction coefficients for a lossless square dielectric object vibrating vertically, along the y-axis, with a relative permittivity of 2, 5 and 7.

#### 4.1.3 Horizontally (along the x-axis) Vibrating Dielectric Wedges

To further understand the influence of the mode of vibration on the Doppler diffraction coefficient, a lossless square dielectric vibrating horizontally, along the x-axis, is implemented. The results of the Doppler diffraction coefficient are shown in Figure 24.

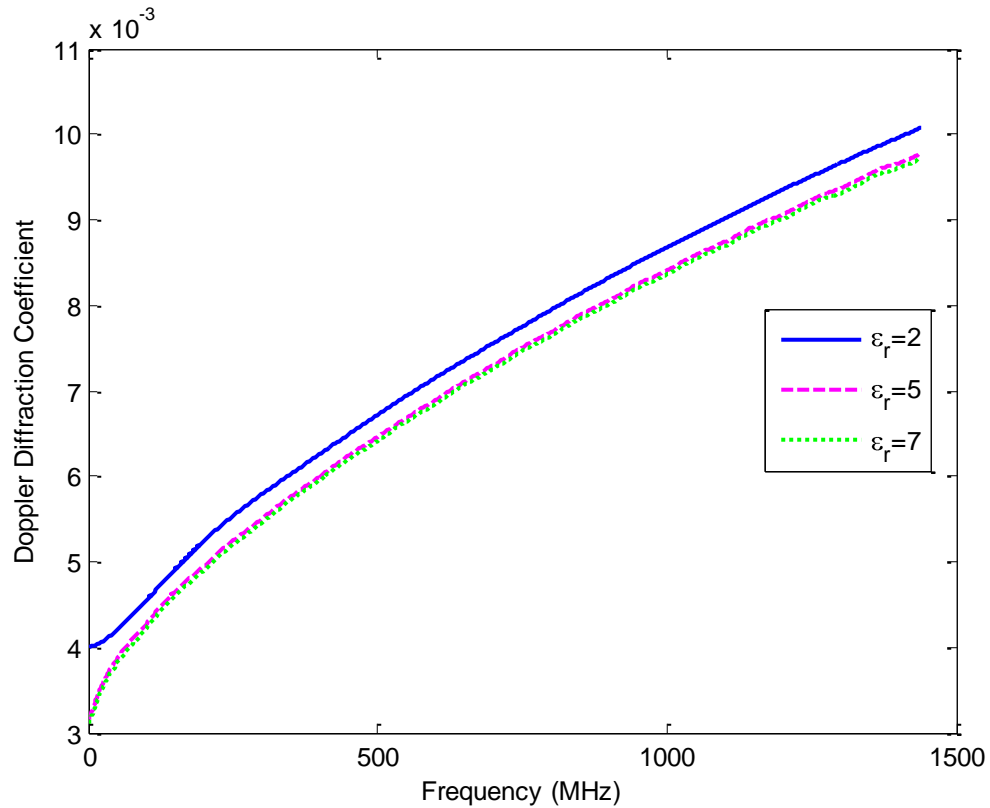


**Figure 24:** Comparison between the Doppler diffraction coefficients for a lossless square dielectric object vibrating horizontally, along the x-axis, with a relative permittivity of 2, 5 and 7.

## 4.2 Diffraction Coefficients of Lossy Wedges

### 4.2.1 Stationary Lossy Wedges

A relationship between the diffraction coefficients of a stationary square dielectric object with losses,  $\sigma=0$ ,  $\sigma=10$ , and a fixed relative permittivity of 7 are shown in Figure 25.

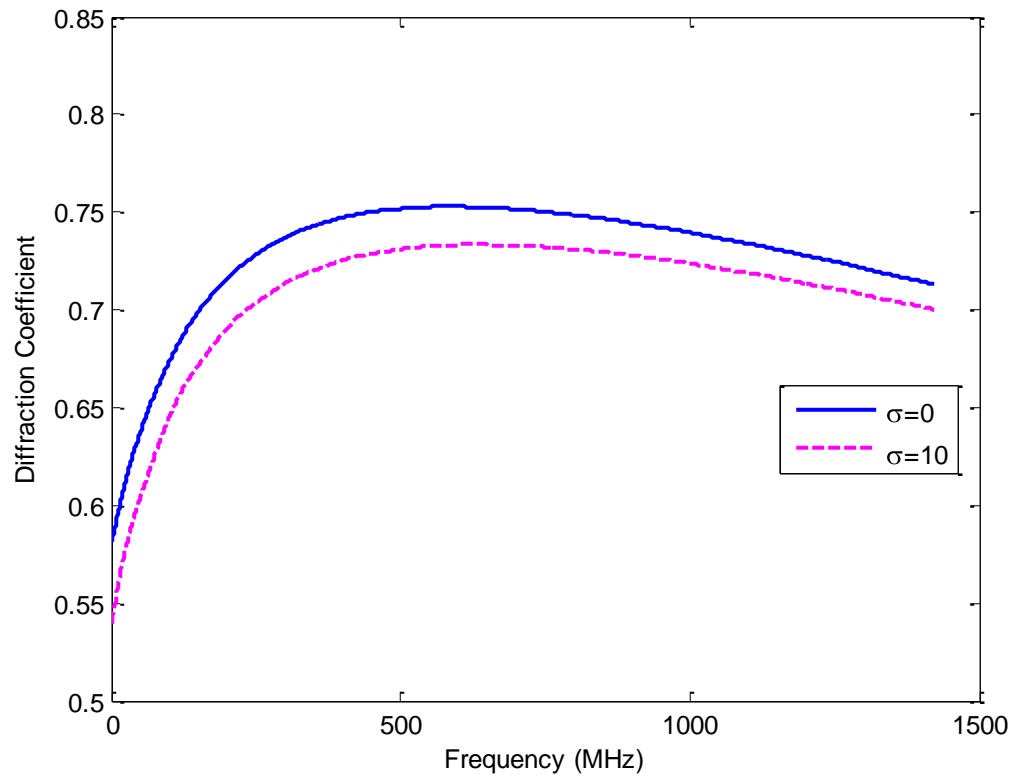


**Figure 25:** Comparison between the diffraction coefficients for a lossy stationary square dielectric object with a fixed relative permittivity of 7 and a conductivity of 0 and 10.

#### 4.2.2 Vertically (along the y-axis) Vibrating Lossy Wedges

The results of the Doppler diffraction coefficient for the lossy square dielectrics with a conductivity of 0 and 10 and a fixed relative permittivity of 7 vibrating vertically, along the y-axis, are displayed in Figure 26.

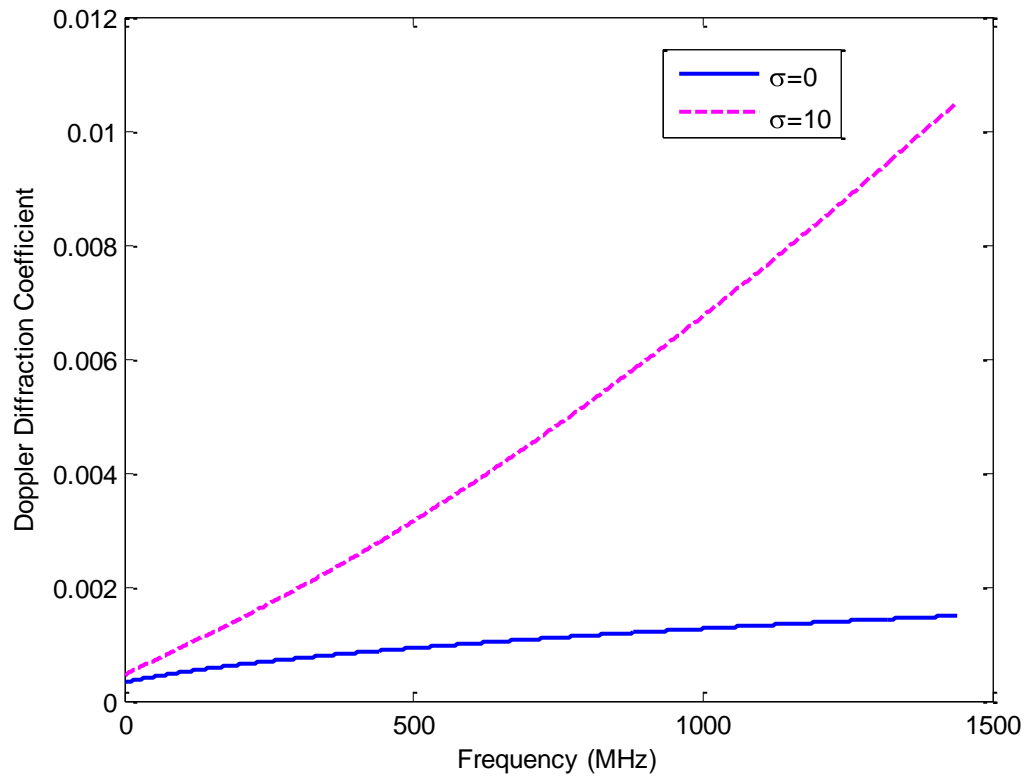


**Figure 26:** Comparison between the Doppler diffraction coefficients for a lossy square dielectric object vibrating vertically, along the y-axis, with a fixed relative permittivity of 7 and a conductivity of 0 and 10.

#### 4.2.3 Horizontally (along the x-axis) Vibrating Lossy Wedges

For the case with the lossy square dielectric with a conductivity of 0 and 10 and a fixed relative permittivity of 7 vibrating horizontally, along the x-axis, the amplitude of the Doppler diffraction coefficients are compared in Figures 27.

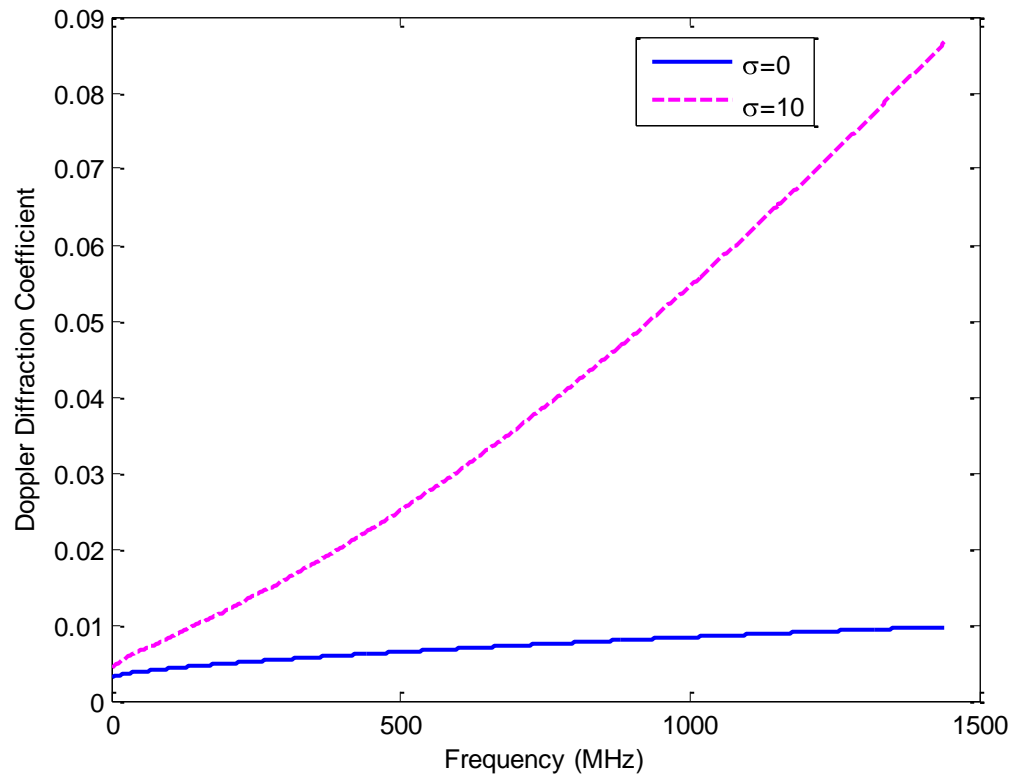


**Figure 27:** Comparison between the Doppler diffraction coefficients for a lossy square dielectric object vibrating horizontally, along the x-axis, with a fixed relative permittivity of 7 and a conductivity of 0 and 10.

## Chapter 5

### Conclusion

In this Thesis, an FDTD code was developed that implements a TFSS incident plane wave formulation, CPML [3] boundary conditions, a frequency-domain NTFF transformation and an advanced SBC [4,5]. Thus, this code is capable of realizing a plane wave incident at various angles, computing remote fields at any angle, implementing a vibrating object and determining the diffraction coefficient from the corner of a stationary and vibrating object.

The results from the FDTD modeling is utilized to better understand the RCS of vibrating objects at different modes and for various materials, which assists in the process of enhancing the knowledge of the interaction of EM pulses and vibrating targets in order to carry out the overall goal of designing SAR imaging strategies that yield two-dimensional (spatial) maps of vibration frequencies (spectrograms) superimposed on ordinary SAR images..

Upon conducting several verification studies, diffraction coefficients for stationary and vibrating lossless and lossy dielectric objects were obtained. The results show that the magnitude of the Doppler diffraction coefficients of a vibrating object having a relative permittivity of 2, 5 or 7 and a conductivity of 10 is lower than the diffraction coefficient from the corresponding stationary object. Also, when comparing the Doppler diffraction coefficients of the object vibrating vertically versus horizontally, the object that is vibrating horizontally has a lower magnitude than the object vibrating vertically.

Although square objects and a right-angle wedges are considered in this Thesis, and straightforward one-dimensional vibrations are implemented, arbitrarily shaped and arbitrarily vibrating objects may be accounted for in the FDTD grid in a straightforward manner. Thus, the FDTD models constructed for this Thesis are very versatile and flexible so that they may be applied to a variety of realistic problems.

## Chapter 6

### Future Work

One of the next goals is to compare the results from the code in this Thesis to the results obtained from experiments in the laboratory. Also, obtaining results using a recently implemented time-domain NTFF for post processing is of great interest so that the received time-domain far-field waveforms may undergo advanced signal processing.

Additionally, an aerial survey with a triangular trihedral target on the ground made of aluminum has already been implemented in the field. Thus, the next steps will be to extend this model to 3-D, model the specific triangular trihedral target made of aluminum along with its movement and obtain the backscattered signal to compare with the measured results.

Extending the modeling to 3-D will greatly increase the practicality and applicability of this model. In the more long-term, an aerial survey giving the radar returns from actual, complex vibrating buildings will be carried out and the 3-D FDTD code will be extended to study this more complex problem.



## REFERENCES

- [1] K. S. Yee, "Numerical solution of initial boundary value problems involving Maxwell's equations in isotropic media," *IEEE Transactions on Antennas and Propagation*, pp. , 302-307, 1966.
- [2] Taflove and S. C. Hagness, *Computational Electrodynamics: The Finite-Difference Time-Domain Method*, 3rd edition. Norwood, MA: Artech House, 2005.
- [3] J. A. Roden and S. D. Gedney, "Convolutional PML (CPML): An efficient FDTD implementation of the CFS-PML for arbitrary media," *Microwave and Optical Technology Letters.*, Vol. 27, p. 334-339, 2000.
- [4] A. Buerkle and K. Sarabandi, "Analysis of acousto-electromagnetic wave interaction using sheet boundary conditions and the finite-difference time-domain method," *IEEE Transactions on Antennas and Propagation*, vol. 55, no. 7, pp. 1991-1998, 2007.
- [5] A. Buerkle and K. Sarabandi, "Analysis of acousto-electromagnetic wave interaction using the finite-difference time-domain method," *IEEE Transactions on Antennas and Propagation*, vol. 56, no. 8, pp. 2191-2199, 2008.
- [6] M. Zhao, J. D. Shea, S. C. Hagness, D. W. van der Weide, B. D. Van Veen and T. Varghese, "Numerical study of microwave scattering in breast tissue via coupled dielectric and elastic contrasts," *IEEE Antennas and Wireless Propagation Letters*, vol. 7, pp. 247-250, 2008.
- [7] C. R. Birtcher, C. A. Balanis and D. DeCarlo, "rotor-blade modulation on antenna amplitude pattern and polarization: Predictions and measurements," *IEEE Transactions on Electromagnetic Capability*, vol. 41, no. 4, pp. 384-393, 1999.
- [8] J. V. Bladel, "Electromagnetic fields in the presence of rotating bodies," *Proceedings of the IEEE*, vol. 64, pp. 301-318, 1976.
- [9] S. R. Borkar and R. F. H. Yang, "Reflection of electromagnetic waves from oscillating surfaces," *IEEE Transactions on Antennas and Propagation*, pp. 122-127, 1975.
- [10] K. Sarabandi and E. Lawrence, "Acoustic and electromagnetic wave interaction: Estimation of Doppler spectrum from an acoustically vibrated metallic circular cylinder," *IEEE Transactions on Antennas and Propagation*, vol. 51, pp. 1499-1507, 2003.
- [11] D. E. Lawrence and K. Sarabandi, "Acoustic and electromagnetic wave interaction: Analytical formulation for acousto-electromagnetic scattering

behavior of a dielectric cylinder," *IEEE Transactions on Antennas and Propagation*, vol. 49, no. 10, pp. 1382-1392, 2001.

- [12] D. E. Lawrence and K. Sarabandi, "Electromagnetic scattering from vibration penetrable objects using a general class of time-varying sheet boundary conditions," *IEEE Transactions on Antennas and Propagation*, vol. 54, no. 7, pp. 2054-2061, 2006.
  
- [13] G. Stratis, V. Anantha and A. Taflove, "Numerical calculation of diffraction coefficients of generic conducting and dielectric wedges using FDTD," *IEEE Transactions on Antennas and Propagation*, vol. 43, no. 10, pp. 1525-1529, 1997.
  
- [14] A. Taflove, "Application of the finite-difference time-domain method to sinusoidal steady-state electromagnetic-penetration problems," *IEEE Transactions on Electromagnetic Compatibility*, vol. EMC-22, no. 3, pp. 191-202, 1980.
  
- [15] C. A. Balanis, "Geometrical Theory of Diffraction," in *Advanced Engineering Electromagnetics*. New York: Wiley, 1989, ch. 13.